SEVENTH FRAMEWORK PROGRAMME

THEME FP7-ICT-2009-C

Instrument	STREP
Project no.	244068
Project acronym	**CROSSTRAP**
Project title	**C**oherently-enhanced **R**aman **O**ne-beam **S**tandoff **S**pectroscopic **TR**acing of **A**irborne **P**ollutants

Deliverable D1.3

Report on High-Energy Filamentation

Due date of deliverable	month 40
Actual submission date	24/06/2013
Start date of project	01/02/2010
Duration of the project	40 months
Organization name of lead contractor for this deliverable	**TU WIEN**
Dissemination Level	public

CROSSTRAP
Deliverable D1.3

SHORT DESCRIPTION:

In the final year of the project, we have significantly deepened our understanding, on both the experimental and theoretical levels, of how coherent UV emission from nitrogen molecules can be obtained as a result of ultrashort pulse filamentation. Whilst the advantages of long-wavelength excitation became apparent earlier in the project and were exploited by using the available 4-µm parametric source, they also clearly identified the mammoth technical challenge of building a very high energy parametric source. To circumvent the pulse energy shortage and to exploit additional control parameters, such as pump pulse duration, the most important results on high-energy filamentation were performed using a multi-Joule laser facility at LLNL. The most significant output of two measuring campaigns at LLNL is a clear evidence for delayed population inversion obtained by collisional excitation of nitrogen molecules by hot electron plasma. Irrefutable evidence for the generation of picosecond 337-nm was obtained and explained by extensive numerical modeling to be the result of gradual population inversion buildup on a picosecond time scale caused by the predominantly collisional heating of free electrons resulting from photoionization. This deliverable provides exhaustive information on the developed numerical model and experimental results of 337-nm generation triggered by Joule-class filamentation in air and pure nitrogen. The remaining part of the report details new evidence for adaptive enhancement of UV emission at the molecular cation transition at 391 nm and suggests distinctly different possible scenarios for lasing action, including the opportunity for femtosecond bursts of laser amplification without inversion during periodic re-phasing of rotational wave-packets of the ground and excited states of the cation.

1_ INTRODUCTION

This report summarizes our understanding of the phenomena leading to coherent UV emission in nitrogen as a result of filamentation of femtosecond pulses at 1.03 and 3.9 µm (internal CROSS TRAP laser sources) and chirped picosecond pulses at 1.05-µm (a multi-Joule laser at LLNL). The report is structured as follows: Part A details the theoretical model of plasma dynamics that is initiated by photoionization during the pump laser pulse and later evolves as free plasma in the presence of several plasma-chemical channels of deactivation. Part B reports on the observation of a delayed population inversion build-up under picosecond excitation with a multi-Joule pump laser and shows a good agreement between the experimental results and the developed kinetic modeling. Finally, part C revisits the molecular cation emission reported in D1.2. Here, we present new experimental results that time-resolve the sequence of UV signal enhancement and show numerically the possibility of periodic laser gain at rotational revivals in a system that does not exhibit population inversion in its classic meaning.

A_ MODELING FOR ASE LASER IN FEMTOSECOND FILAMENTS

To formulate requirements to laser sources generating filament for standoff lasing initiation in the atmosphere, we have developed, in collaboration with Prof. M. Shneider from Princeton University, a numerical model which allows studying plasma kinetics under femtosecond filamentation conditions. Molecular nitrogen provides effective UV lasing at several wavelengths, with 337 nm, 357 nm and 380 nm being the strongest transitions, when population inversion between two excited electronic states $C^3\Pi_u$ and $B^3\Pi_g$ is achieved. The specifics of molecular nitrogen as a laser gain media is that the excitation step from the ground $X^1\Sigma_g$ electronic state to the lasing levels, which we will refer to further as C and B states, cannot be accomplished by optical pump because these excitations are strongly forbidden by the spin conservation law. Correspondingly, molecular nitrogen laser is a discharge pumped type of gas lasers where population inversion builds up via collisional pumping by high energy electrons. It is investigated in detail both experimentally and theoretically under the conditions of a dc or an impulsive discharge [Kunabenchi84]. Naturally, plasma kinetics and, specifically, the density and the temperature of electrons play the key role in the population dynamics of the electronic states.

In spite of large similarity in the physical picture of plasma kinetics between an rf/dc discharge and an optical breakdown by ultrashort laser pulses, there are several principal differences. Under the conditions of impulsive rf- or capacitor discharge, rapid Joule heating of electrons due to collisions with neutrals leads to the formation of a non-equilibrium energy distribution of electrons [Raizer]. The energy distribution and the plasma concentration are maintained throughout the discharge on a microsecond time scale resulting in a sufficient amount of hot electrons with kinetic energies around 15 eV—the peak of the excitation cross-section for the C-state—needed for efficient pumping of the C state.

By contrast, in a laser filament, the electronic energy distribution is formed on the time scale of the femtosecond laser pulse by the optical field ionization process. After the femtosecond pulse, the resultant energy distribution function evolves freely as the plasma concentration decays. Therefore, the required excitation of the C state by electron impact can only be achieved within a sub-ns time scale of the electronic density decay in air [Bodrov11]. The effect of intensity clamping, set by the dynamic interplay between self-focusing and plasma refraction, limits the laser intensity in the filament and the filament diameter [Couairon07] and precludes the possibility of direct scaling of the electronic temperature in a filament via an increase of the pulse energy.

Our model of plasma kinetics in a femtosecond filament shows that the laser wavelength is the key parameter which enables control over the initial electronic temperature in the filament plasma. The model consists of kinetic equation for electron energy distribution function (EEDF) and the system of rate equations describing population of different electronic states.

A1. Kinetic equation for electronic energy distribution function

We use the well-known in discharge physics two-term (Lorentz) approximation to the solution of the Boltzmann kinetic equation for the electronic energy distribution function (EEDF) [Raizer]. In this approximation the solution is presented in the form of the first two members of Legendre polynomials expansion $F(\varepsilon) = f(\varepsilon, t) + f_1(\varepsilon, t)cos\theta$. Substituting this expression into the Boltzmann kinetic equation, we derive the following kinetic equation for the isotropic part of the EEDF, describing the electronic energy spectrum:

$$\frac{\partial f}{\partial t} = \frac{\partial}{\partial \varepsilon}([0.79\delta_1\nu_1(\varepsilon) + 0.21\delta_2\nu_2(\varepsilon)]\varepsilon f) + \frac{\partial J_{ee}}{\partial \varepsilon} + Q(f) \qquad \text{(A1)}$$

Here ε is electronic kinetic energy, $\delta_{1,2}=2m/M_{1,2}$ where m is the mass of electron and $M_{1,2}$ are the masses of nitrogen and oxygen molecules, $\nu_{1,2}(\varepsilon)$ are frequencies of electronic elastic collisions with nitrogen and oxygen molecules correspondingly, J_{ee} is the electron flux over the energy axis related to the Coulomb electron-electron collisions and modeled according to [Rockwood73], $Q(f)$ describes inelastic electron-molecule collisions. The coefficients 0.79 and 0.21 are the volume fractions of nitrogen and oxygen molecules in the atmosphere. The frequency of electronic collisions with molecules can be expressed via experimentally measurable collision cross-sections as follows: $\nu(\varepsilon) = 5.93 \cdot 10^7 N\sigma(\varepsilon)\sqrt{\varepsilon}$ where N is the molecular density, $\sigma(\varepsilon)$ is collision cross-sections and electronic energy is measured in eV. The energy dependent cross-sections of **elastic electronic collisions** with nitrogen and oxygen molecules where taken as the recommended values from [Itikawa06, Itikawa09].

In our model we take into account the following **inelastic collisional processes**:

a) **Electron impact excitations** of different electronic states in a nitrogen molecule. The following electronically excited states are considered: $A^3\Sigma_u$, $B^3\Pi_g$, $a^1\Sigma_u$, $a^1\Pi_g$, $C^3\Pi_u$. The corresponding excitation cross-sections are taken from [Itikawa06]. The corresponding source of inelastic energy losses in the right side of (1) can be expressed as follows:

$$Q_{exc}(\varepsilon, f) = \left[\begin{array}{c} f(\varepsilon+E)\nu_{ee}(\varepsilon+E),\ \varepsilon < E \\ f(\varepsilon+E)\nu_{ee}(\varepsilon+E) - f(\varepsilon)\nu_{ee}(\varepsilon),\ \varepsilon \geq E \end{array}\right. \qquad \text{(A2)}$$

where E is the excitation energy of an electronic state and excitation frequency $\nu_{ee}(\varepsilon)=0$ for energies $\varepsilon<E$.

b) **Super-elastic electronic scattering** on electronically excited nitrogen molecules. The corresponding collisional cross-sections are taken from [Bacri82] and excitation energies are given in Tab.1. When an electron scatters on an electronically excited nitrogen molecule, it can either excite it further to a higher lying state losing the energy or the electron can gain the excitation energy of the state and de-excite it to a lower lying state. The cross-sections of the electron impact excitation and de-excitation channels between two selected states are the same. However, the corresponding population rates are different, as will be discussed below.

Table A1. Excitation energies for different electronics states in molecular nitrogen [Itikawa06]

	$A^3\Sigma_u$	$B^3\Pi_g$	$a^1\Sigma_u$	$a^1\Pi_g$	$C^3\Pi_u$
$X^1\Sigma_g$	7.6	8.5	9	7.9	10.9
$A^3\Sigma_u$		0.9	2.4	2.4	4.9
$B^3\Pi_g$			0.9	1.4	3.4
$a^1\Sigma_u$				0.9	2.4
$a^1\Pi_g$					2.4

The corresponding source in the right side of Eq.A1, describing the inelastic energy losses by electrons in super-elastic collisions with excitation from the i^{th} electronic state to the j^{th} electronic state, can be expressed as follows:

$$Q_{ij}(\varepsilon,f) = \begin{cases} f(\varepsilon+E_{ij})\nu_{se}(\varepsilon+E_{ij}), \ \varepsilon < E_{ij} \\ f(\varepsilon+E_{ij})\nu_{se}(\varepsilon+E_{ij}) - f(\varepsilon)\nu_{se}(\varepsilon), \ \varepsilon \geq E_{ij} \end{cases} \qquad \text{(A3)}$$

where E_{ij} is the energy for excitation and excitation frequency $\nu_{se}(\varepsilon)=0$ for energies $\varepsilon<E_{ij}$. The source for super-elastic collisions leading to electronic de-excitations from the j-electronic state to the i^{th} electronic state can be described as follows:

$$Q_{ji}(\varepsilon,f) = \begin{cases} -f(\varepsilon)\nu_{se}(\varepsilon), \ \varepsilon < E_{ij} \\ f(\varepsilon-E_{ij})\nu_{se}(\varepsilon-E_{ij}) - f(\varepsilon)\nu_{se}(\varepsilon), \ \varepsilon \geq E_{ij} \end{cases} \qquad \text{(A4)}$$

c) **Vibrational excitation of nitrogen and oxygen molecules** by electron impact. The corresponding cross-sections were taken from [Itikawa06]. The corresponding source of inelastic energy losses in the right side of (1) can be expressed as follows:

$$Q_{vib}(\varepsilon,f) = \begin{cases} f(\varepsilon+E)\nu_{ev}(\varepsilon+E), \ \varepsilon < E \\ f(\varepsilon+E)\nu_{ev}(\varepsilon+E) - f(\varepsilon)\nu_{ev}(\varepsilon), \ \varepsilon \geq E \end{cases} \text{(A5)}$$

where E is the vibration excitation energy of a vibrational state and excitation frequency $\nu_{ev}(\varepsilon)=0$ for energies $\varepsilon<E$.

d) **Electron impact ionization** of nitrogen and oxygen molecules. The corresponding cross-sections for electron impact ionization from the ground state in molecular nitrogen and oxygen are taken from [Itikawa06, Itikawa09]. The cross-sections from electronically excited states of nitrogen are taken from [Bacri82]. Depending on electrons energy, molecular ion in different electronic states might be created as a result of a collision. To calculate the total electron impact ionization cross-sections for each electronic state in neutral molecular nitrogen, we sum over all accessible final states of the molecular ion. These cross-sections are integrated over the energy of the secondary electron released in an ionizing collision. To model the inelastic source in the right side of (A1) describing energy losses and appearance of new electrons due to impact ionization, we follow the approach developed in [Raizer]:

$Q_{ion}(\varepsilon,f) = -f(\varepsilon)\nu_i(\varepsilon) + \int_{\varepsilon+I_p}^{\infty} f(\acute{\varepsilon})\nu_i(\acute{\varepsilon})\left[\Phi(\varepsilon',\varepsilon) + \Phi\left(\acute{\varepsilon},\ \acute{\varepsilon}-\varepsilon-I_p\right)\right]d\acute{\varepsilon}$. Here $\Phi(\varepsilon',\varepsilon)$ is the probability for the secondary electron, released by the primary electron with the energy ε′, to have an energy in the interval ε to ε+dε. Assuming that the residual energy of the impinging electron, after subtraction of the ionization potential, is shared equally with the secondary electron, $\Phi(\varepsilon',\varepsilon)$ can be presented as $\Phi(\varepsilon',\varepsilon) = \delta\left(\varepsilon - \frac{\acute{\varepsilon}-I_p}{2}\right)$. The ionization inelastic source then can be written as:

$$Q_{ion}(\varepsilon,f) = \left[\begin{array}{c} 4f(2\varepsilon+I_{pi})\nu_i(2\varepsilon+I_{pi}),\ \varepsilon < I_{pi} \\ 4f(2\varepsilon+I_{pi})\nu_i(2\varepsilon+I_{pi}) - f(\varepsilon)\nu_i(\varepsilon),\ \varepsilon \geq I_{pi} \end{array}\right. \qquad \text{(A6)}$$

where I_{pi} is ionization potential for i-electronic state and impact ionization frequency $\nu_i(\varepsilon)=0$ for energies $\varepsilon<I_{pi}$.

e) **Electron-ion recombination**. We used temperature dependent recombination rates measured in [Kossyi92]. Dissociative recombination of an electron with a nitrogen molecular ion has two reaction channels. The first channel is $N_2^+ + e \rightarrow N + N$, providing dissociation products in the ground electronic state, has the reaction rate $\beta_{1N} = 4.5\cdot10^{-8}T^{-1/2}$ where $T = \frac{2}{3}\frac{\int_0^{\infty}\varepsilon f(\varepsilon)d\varepsilon}{\int_0^{\infty}f(\varepsilon)d\varepsilon}$ is the "average" electronic temperature calculated from (1). The second channel is $N_2^+ + e \rightarrow N + N(^2D)$ with the reaction rate $\beta_{2N} = 3.2\cdot10^{-8}T^{-1/2}$. Dissociative recombination of electrons with molecular oxygen ions $O_2^+ + e \rightarrow O + O$ has the reaction rate $\beta_O = 3.2\cdot10^{-8}T^{-1/2}$. The corresponding source of electron losses in the right side of (1) can be expressed as follows:

$$Q_{rec}(\varepsilon) = -[(\beta_{1N}+\beta_{2N})N_{N+} + \beta_O N_{O+}]f \qquad \text{(A7)}$$

where N_{N+} and N_{O+} are densities of nitrogen and oxygen molecular ions.

The total inelastic source in the right side of (1) is the sum over all above mentioned channels: $Q(f) = \sum_{i\neq j} Q_{ij}^{exc} + \sum_{j\neq i} Q_{ji}^{deexc} + Q_{vib} + \sum_i Q_{ion}^i + Q_{ion}^{oxygen} + Q_{rec}$ where indexes i,j enumerate electronic states in nitrogen or oxygen.

A2. Photoionization source in the kinetic equation.

As was mentioned above, plasma formation in a femtosecond filament occurs on the femtosecond time scale of the optical pulse. Therefore, the initial EEDF is a solution of quantum-mechanical problem of gas ionization by high intensity ultrashort laser pulse. **Dependence of conditions for population inversion and entire plasma dynamics in the filament on the laser wavelength is entirely determined by this solution.** Full 3D numerical simulations of this problem are extremely challenging and such results for molecular gases are not known. To find actual ionization rates for molecular species in air, we use the analytical formalism developed in [Perelomov66] with empirical corrections experimentally determined in [Talebpour99]. Ionization rate (in s^{-1}) for molecular nitrogen and oxygen is calculated as follows:

$$R(E) = \sqrt{\frac{6}{\pi}}\frac{eE_H}{\sqrt{2m_eW_H}}\left|C_{n^*,l^*}\right|^2 f(l,m)\frac{W_i}{2W_H}A_m(\gamma)\left(\frac{2E_0}{E\sqrt{1+\gamma^2}}\right)^{2n^*-|m|-3/2} exp\left(-\frac{2E_0}{3E}g(\gamma)\right) \quad \text{(A8)}$$

where $\gamma = \frac{\omega\sqrt{2mW_i}}{eE} = \sqrt{\frac{W_i}{2U_p}}$ is the Keldysh parameter, ω and E are the frequency and electric filed in the laser pulse, W_i is the gas ionization potential, U_p is the pondermotive energy, $E_0 = E_H(W_i/W_H)^{3/2}$ is the effective atomic electric field, W_H=13.6 eV is the hydrogen ionization potential, E_H=5.14 GV/cm is the electric field in the hydrogen atom, $n^* = Z\sqrt{W_i/W_H}$ is the effective principal quantum number, $l^*=n^*-1$ is the effective orbital quantum number, l and m are the orbital and magnetic quantum numbers. The coefficient $\left|C_{n^*,l^*}\right|^2$ is defined as $\left|C_{n^*,l^*}\right|^2 = \frac{2^{2n^*}}{n^*\Gamma(n^*+l^*+1)\Gamma(n^*-l^*)}$ where Γ is the gamma-function, the coefficient $f(l,m)$ is defined as $f(l,m) = \frac{(2l+1)(l+|m|)!}{2^{|m|}(|m|)!(l-|m|)!}$. The functions $A_m(\gamma)$ and $g(\gamma)$ are defined as $A_m(\gamma) = \frac{4}{\sqrt{3}\pi}\frac{1}{|m|!}\frac{\gamma^2}{1+\gamma^2}\sum_{\kappa>\nu}^{\infty} exp(-(\kappa-\nu)\alpha(\gamma))\,\Phi_m\left(\sqrt{(\kappa-\nu)\beta(\gamma)}\right)$ where $\nu = \frac{W_i}{\hbar\omega}\left(1+\frac{1}{2\gamma^2}\right)$ and κ is the nearest integer above ν, $\Phi_m(x) = e^{-x^2}\int_0^x (x^2-y^2)^{|m|}e^{y^2}dy$, $\alpha(\gamma) = 2\left(\sinh^{-1}\gamma - \frac{\gamma}{\sqrt{1+\gamma^2}}\right)$, $\beta = \frac{2\gamma}{\sqrt{1+\gamma^2}}$, $g(\gamma) = \frac{3}{2\gamma}\left[\left(1+\frac{1}{2\gamma^2}\right)\sinh^{-1}\gamma - \frac{\sqrt{1+\gamma^2}}{2\gamma}\right]$.

This ionization rate, integrated over the duration of the filamentation pulse, provides relative contributions to ionization of nitrogen and oxygen and the total amount of plasma generated in the filament. To get a good agreement between the ion yield in nitrogen and oxygen calculated by (9) and measured experimentally in femtosecond filament generated by 800 nm wavelength laser pulses, the following parameters where suggested in [Talebpour99]: W_i=15.58 eV and Z=0.9 for molecular nitrogen and W_i=12.55 eV and Z=0.53 for molecular oxygen.

Also in frame of the PPT model of strong field ionization, the energy distribution function of photoelectrons was derived analytically in [Mur01] for arbitrary values of Keldysh parameters and an arbitrary polarization in the laser electric field. We use this expression for linearly polarized field in the femtosecond filament to calculate the initial condition for the equation (Eq. A1):

$$f_0(\varepsilon) = 2\pi A(\varepsilon)\sqrt{2m\varepsilon}\int_{-1}^{1} du\, exp\{-2\varepsilon(c_1(1-u^2)+c_2u^2)\} \times$$
$$exp\{-c(\varepsilon)(1-u^2)\}I_0\{c(\varepsilon)(1-u^2)\} \quad \text{(A9)}$$

where $c_1 = t_0 - \tanh t_0$, $c_2 = t_0$, $t_0 = \ln(1+\sqrt{1+\gamma^2})$, $c(\varepsilon) = \varepsilon \tanh t_0$, I_0 is the modified Bessel function and function $A(\varepsilon) = \frac{\hbar\omega}{\sqrt{U_p(1+\gamma^2)}}\exp(-\frac{W_i}{\hbar\omega}g(\varepsilon))$, $g(\varepsilon) = \frac{1}{\sqrt{2}}\left(\left(1+\frac{1}{2\gamma^2}\right)t_0 - \frac{\sqrt{1+\gamma^2}}{2\gamma}\right)$.

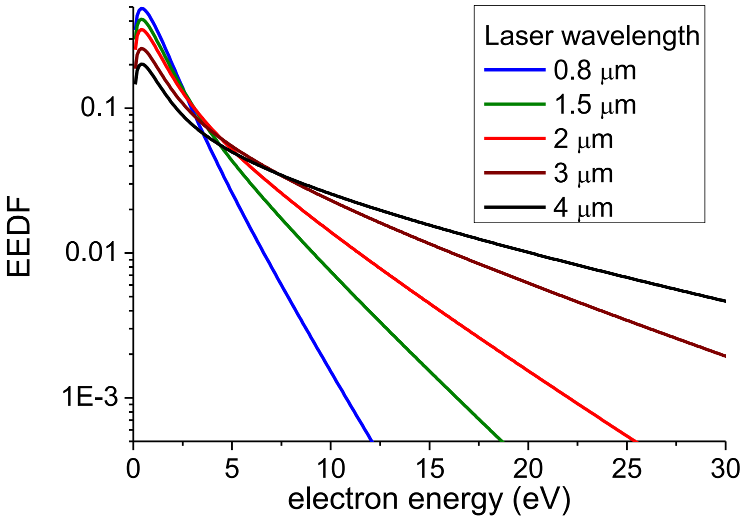

Fig. A1. Energy distribution function of photo-electrons calculated by (Eq. A9) for different wavelengths of a laser generating the filament.

The analytical solution (Eq. A9), together with the rate (Eq. A8), provides the initial EEDF for the kinetic equation (1). The calculated energy distribution for photoelectrons generated in the filament with the fixed laser intensity 4·10^{13} W/cm^2 and different laser wavelengths is presented in Fig.A1. In the tunnel ionization limit $\gamma \ll 1$ (Eq. A9) has an approximate analytical solution $f_0(\varepsilon) \propto exp\left\{-\frac{2}{3}\gamma^3\frac{\varepsilon}{\hbar\omega}\right\}$ [Mur01]. Therefore, the initial effective electronic temperature $T_e \propto \hbar\omega/\gamma^3 \propto \lambda^2$, meaning that **the longer wavelength filament provides hoter plasma**, as confirmed by Fig. A1.

A3. Kinetic processes involved and corresponding rate equations

Electrons in the femtosecond filament plasma cools down and vanish on the time scale about 1 ns [Bodrov11]. Analyzing the population dynamics of different excited electronic states in molecular nitrogen on this time scale, we take into account the following channels of collisional quenching:

a) collisional quenching of the $C^3\Pi_u$ state (the upper lasing level in nitrogen laser)

$N_2(C^3\Pi_u) + N_2(X^1\Sigma_g) \rightarrow N_2(a^1\Sigma_u) + N_2(X^1\Sigma_g)$

with the rate $\beta_{qC1}=10^{-11}$ cm^3/s;

b) collisional quenching of the $C^3\Pi_u$ state

$N_2(C^3\Pi_u) + O_2 \rightarrow O + O + N_2(X^1\Sigma_g)$

with the rate $\beta_{qC2}=3\cdot 10^{-10}$ cm^3/s;

c) collisional quenching of the $B^3\Pi_g$ (the lower lasing level in nitrogen laser) state

$N_2(B^3\Pi_g) + O_2 \rightarrow O + O + N_2(X^1\Sigma_g)$

with the rate $\beta_{qB1}=3\cdot 10^{-10}$ cm^3/s;

d) collisional quenching of the $B^3\Pi_g$ state

$N_2(B^3\Pi_g) + N_2(X^1\Sigma_g) \rightarrow N_2(A^3\Sigma_u) + N_2(X^1\Sigma_g)$

with the rate $\beta_{qB2}=5\cdot 10^{-11}$ cm^3/s [Kossyi92].

In the rate equations for the $N_2(B^3\Pi_g)$ and $C^3\Pi_u$ states, we take into account also the spontaneous emission population decay channel with the rate $1/\tau_s$ where the spontaneous emission life-time is 36 ns for a very low pressure. The lifetime of spontaneous emission scales with pressure *P* as $\tau_s = \frac{36}{1+12.8\cdot P}$ [Lofthus77], so that at normal pressure τ_s is reduced to just ~2 ns. The system of the rate equations then is:

a) **For electronic states in molecular nitrogen** $X^1\Sigma_g$, $A^3\Sigma_u$, $B^3\Pi_g$, $a^1\Sigma_u$, $a^1\Pi_g$, $C^3\Pi_u$ correspondingly:

$$\frac{dN_0}{dt} = -\left(R_0^i + \sum_{j=1}^{5} R_{0j}\right)N_0 + \sum_{j=1}^{5} R_{j0}N_j + \left(\beta_{qC2}N_5 + \beta_{qB1}N_2\right)N_{O_2} + \beta_{qB2}N_2N_0$$

$$\frac{dN_1}{dt} = -\left(R_1^i + \sum_{j=0,j\neq 1}^{5} R_{1j}\right)N_1 + \sum_{j=0,j\neq 1}^{5} R_{j1}N_j$$

$$\frac{dN_2}{dt} = -\left(R_2^i + \sum_{j=0,j\neq 2}^{5} R_{2j}\right)N_2 + \sum_{j=0,j\neq 2}^{5} R_{j2}N_j + R_{st}N_{ph}(N_5 - N_2) - \beta_{qB1}N_2N_{O_2} - \beta_{qB2}N_2N_0$$

$$\frac{dN_3}{dt} = -\left(R_3^i + \sum_{j=0,j\neq 3}^{5} R_{3j}\right)N_3 + \sum_{j=0,j\neq 3}^{5} R_{j3}N_j + \beta_{qC1}N_5N_0$$

$$\frac{dN_4}{dt} = -\left(R_4^i + \sum_{j=0,j\neq 4}^{5} R_{4j}\right)N_4 + \sum_{j=0,j\neq 4}^{5} R_{j4}N_j + \beta_{qC1}N_5N_0$$

$$\frac{dN_5}{dt} = -\left(R_5^i + \sum_{j=0,j\neq 5}^{5} R_{5j}\right)N_5 + \sum_{j=0,j\neq 5}^{5} R_{j2}N_j - R_{st}N_{ph}(N_5 - N_2) - N_5/\tau_s - \beta_{qC2}N_5N_{O_2} - \beta_{qC1}N_5N_0$$

Here R_j^i are the electron impact ionization rates.

b) **For molecular oxygen**:

$$\frac{dN_{O_2}}{dt} = -\left(R_{Oi} + \beta_{qC2}N_5 + \beta_{qB1}N_2\right)N_{O_2}$$

c) **For molecular ions**:

$$\frac{dN_{N^+}}{dt} = \sum_{j=0}^{5} R_j^i N_j - (\beta_{1N} + \beta_{2N}) N_{N^+} N_e$$

$$\frac{dN_{O^+}}{dt} = R_{Oi} N_{O_2} - \beta_O N_{O^+} N_e$$

d) **For atomic oxygen and nitrogen**:

$$\frac{dN_O}{dt} = (\beta_{qC2} N_5 + \beta_{qB1} N_2) N_{O_2} + \beta_O N_{O^+} N_e$$

$$\frac{dN_N}{dt} = (\beta_{1N} + \beta_{2N}) N_{N^+} N_e$$

The system of rate equations (a)-(d) naturally conserves the total amount of particles: $\sum_{j=0}^{5} N_j + N_O + N_N + \frac{1}{2}(N_e + N_{O^+} + N_{N^+}) = const$. This system is solved self-consistently with the kinetic equation (Eq. A1). After each time evolution step, the calculated EEDF is used to obtain the excitation rates $R_{ij} = N_e \int_0^\infty f(\varepsilon)\sqrt{\varepsilon}\sigma_{ij}(\varepsilon) d\varepsilon$, i<j where $N_e = \int_0^\infty f(\varepsilon) d\varepsilon$ and electron impact ionization rates $R_j^i = N_e \int_0^\infty f(\varepsilon)\sqrt{\varepsilon}\sigma_j^i(\varepsilon) d\varepsilon$. De-excitation rates are calculated using the detail balance principle: $R_{ji} = R_{ij} exp\{-\Delta_{ij}/T_e\} g_j/g_i$ where Δ_{ij} is the corresponding excitation energy, $g_{i,j}$ are statistical weights of the states. Calculated populations are used on the next step to solve (A1).

ASE emission

The very important feature of the femtosecond filament driven nitrogen laser is that it operates in the travelling pump regime. A several tenses of centimeters long filament is created by the high power femtosecond pulse on the nanosecond time scale. As it will be shown in the numerical simulations section, the population inversion is reached within several ten to few hundred picoseconds depending on plasma density in the filament. Hence, the filament formation and population inversion build up occur on a similar time scales. Under these conditions, the kinetic equation (Eq. A1) and the system of the rate equations should be expressed in terms of the time in the reference frame of the filamentation pulse. To calculate the generated ASE intensity, we adopt the approach developed for ASE lasers [Hunter81, Haag83] and used before for calculating the yield of optically pumped X-ray lasers [Lin98, Lin99]:

$$\frac{dI^+(z,\tau)}{dz} = \frac{g_0(\tau)}{1+(J^+ + J^-)/J_s} I^+ + A(z,\tau)$$

$$\frac{\partial I^-}{\partial z} - \frac{2}{c}\frac{\partial I^-}{\partial \tau} = \frac{g_0(\tau)}{1+(J^+ + J^-)/J_s} I^- + A(z,\tau) \qquad \text{(A10)}$$

Here I^+ is the ASE intensity emitted in the co-propagating with the filament pulse direction, I^- is the backward propagating ASE, $g_0(\tau) = \Delta N(\tau)\sigma_{emis}$ is the small signal gain, $\tau = t - z/c$ is the time in the reference frame of the filamentation pulse, $\Delta N(\tau)$ is the population inversion obtained from the solution of the equation (A1) with the rate equations, J_s is the saturation fluence, $J = \int_{-\infty}^{t} I(t')dt'$ is the fluence, and the last term is the spontaneous emission source $A(z,\tau) = \frac{\pi}{4}\left(\frac{D}{L}\right)^2 \frac{\hbar\omega\Delta N(\tau)}{1+(I^+ + I^-)/I_s}$ where D and L are the filament diameter and total length. To simplify the system (A10), we note that a large difference in the gain between the forward and the backward directed emission is expected. Indeed, the forward propagating ASE photon starts shortly after the filamentation pulse and it is fed at each propagation point by a freshly created population inversion in the wake of the filament pulse. Taking into account a pretty high value of the stimulated emission cross-section $\sigma_{emis} \approx 4.5 \cdot 10^{-15}$ cm^2 of the C-B nitrogen transition [Papakin85] and relatively short lifetime of the upper lasing level about 2 ns, we estimate the saturation fluence J_s=130 μJ/cm^2. Our simulations show that forward propagating ASE might reach saturation level relatively fast. In contrast, the backward propagating ASE photon propagates in the decaying plasma which limits the effective gain length. These arguments allow us to split the system (A10) into two decoupled equations for the forward and backward waves assuming that saturation (when occurs) is caused by the forward propagating emission. Then the system (A10) can be expressed as:

$$\frac{dI^+(z,\tau)}{dz} = \frac{g_0(\tau)}{1+J^+/J_s} I^+ + A(z,\tau)$$

$$\frac{\partial I^-}{\partial z} - \frac{2}{c}\frac{\partial I^-}{\partial \tau} = \frac{g_0(\tau)}{1+J^+/J_s} I^- + A(z,\tau) \qquad \text{(Eq. A11)}$$

and the forward and the backward ASE pulses can be calculated independently.

A3. Numerical simulations

Plasma density and the laser intensity are the key parameters determining the possibility to achieve population inversion in the filament afterglow. Published experimental measurements of plasma density are referring to the 800 nm wavelength and there are no so far measured values for mid-IR filaments. For 800 nm near-IR wavelength laser sources, plasma density varies in the broad range from 10^{15} to 10^{17} cm^{-3} depending on focusing conditions and laser power [Couairon07]. The laser pulse intensity in the near-IR filament is fixed at the level 2-6·10^{13} W/cm^2 – the phenomenon known as "intensity clamping" and related to the fact that the filament is the product of a dynamical balance between self-focusing and plasma refraction and sustain fixed optical power only. Again, there are no experimental data about the value of intensity clamping for mid-IR filaments. Our numerical simulations for mid-IR filamentation in nitrogen show that the intensity in the filament created by 4 μm wavelength mid-IR femtosecond laser pulses reaches similar values as in the case of near-IR filaments. For comparison between difference laser wavelengths, we have fixed the laser intensity clamping at 4·10^{13} W/cm^2 level and the plasma density at 2·10^{17} cm^{-3} value (less than 1% from the concentration of neutrals in air).

Results of calculations for population inversion are presented in Fig. A2. As follows from Fig. A2, population inversion in femtosecond filament created by a linearly polarized laser pulse can be achieved only for laser wavelength close to 4 μm and longer. To understand the laser wavelength dependence of population inversion, we have investigated a mechanism of population inversion build up. The early time evolution of EEDF is presented in Fig. A3a. The very hot electrons with energies above 11 eV, necessary for direct electron impact excitation from the ground electronic state in molecular nitrogen to the upper lasing C-state (see Tab. A1), vanish via inelastic collisions within the first several picoseconds. As a result, the direct channel of excitation from the ground state to the C-state, which is the main pumping mechanism in the conventional discharge-pumped nitrogen laser [Kunabenchi84], is not effective in the filament.

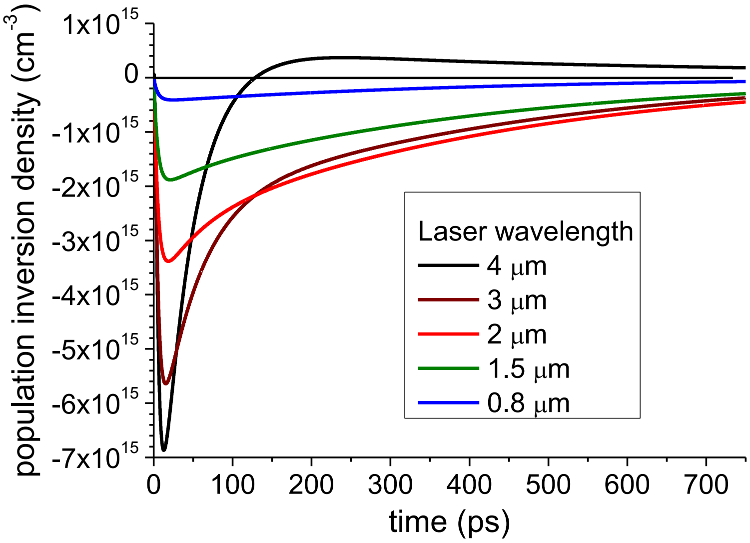

Fig. A2. Time dependence of the population inversion for different filamentation wavelengths.

Population of the C-state proceeds via cascaded mechanism, also known in the conventional discharge-pumped nitrogen laser as playing the minor role [Kunabenchi84]. The first step in this cascaded channel is population of the A-state by electrons with energies above 8 eV (see Tab.1) and occurs within the first several tenses of picoseconds (Fig. A3b). The second step is population of the C-state by superelastic collisions of excited nitrogen molecules in the A-state with electrons having energies above 5 eV (Tab.1). Since the cross-section of electron impact excitation from the A-state to the C-state is higher than the one to the B-state, population inversion is reached after about 150 ps of plasma evolution (Fig. A3b). Requirements to electron energies enabling the cascaded mechanism of population inversion explain the difference in the results for different filamentation laser wavelengths. Initial plasma in the 0.8 μm-laser filament is too cold (see Fig. A1 and Fig. A4a) and cannot provide efficient pumping even if the plasma concentration would be increased twice.

When laser wavelength increases, the initial plasma temperature increases ~λ² (Fig. A4a) and enables cascaded population mechanism for λ≈4 μm. For long wavelength filaments the initial plasma concentration can even increase slightly due to electron-impact ionization from the ground and excited electronic states in neutral molecules (Fig. A4b). It is worth mentioning that the electronic density and temperature decay in our simulations are in a good agreement with experiment and simulations of other groups [Bodrov11].

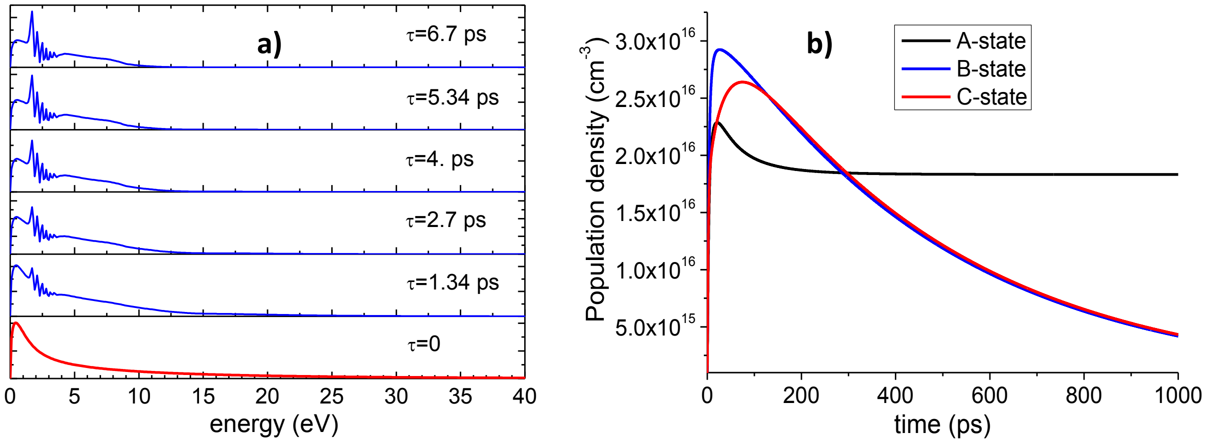

Fig. A3. a) Temporal evolution of the EEDF in afterglow of the 4 μm filament. b) Temporal evolution of the A- and C-state population in afterglow of the 4 μm, 2 μm and 0.8 μm filament.

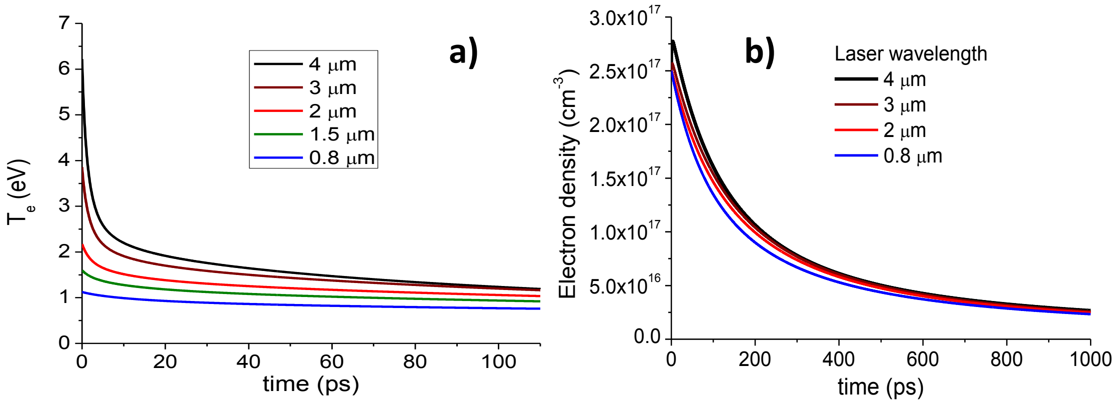

Fig. A4. a) Time-dependent electronic temperature and b) time-dependent electronic density in filament afterglow.

The problem of an insufficient initial plasma temperature might be solved using circularly polarized laser beam for filamentation. In this case, plasma temperature is much higher than for linearly polarized pulse with the same intensity and the entire initial EEDF is shifted to $4U_P$ electron energy [Mur01]. This might be a solution to achieve population inversion with wavelengths shorter than 4 μm. However, for 0.8 μm filament-igniting laser it will be unlikely the case because for typical filament intensities the maximum plasma temperature is still about 3 eV which is not enough for triggering the cascaded population mechanism.

We calculated the intensity of the forward generated UV emission from the ASE nitrogen laser initiated by the 4 μm filament. The results are shown in Fig. A5. Peak intensity of the ASE grows exponentially and reaches saturation for filament length 10 cm. The small signal gain retrieved from simulations is ≈1.5 cm^{-1}. For 20 cm long filament the peak intensity reaches 35 MW/cm^2 and the total generated UV energy in the 100 μm diameter filament is ≈100 nJ.

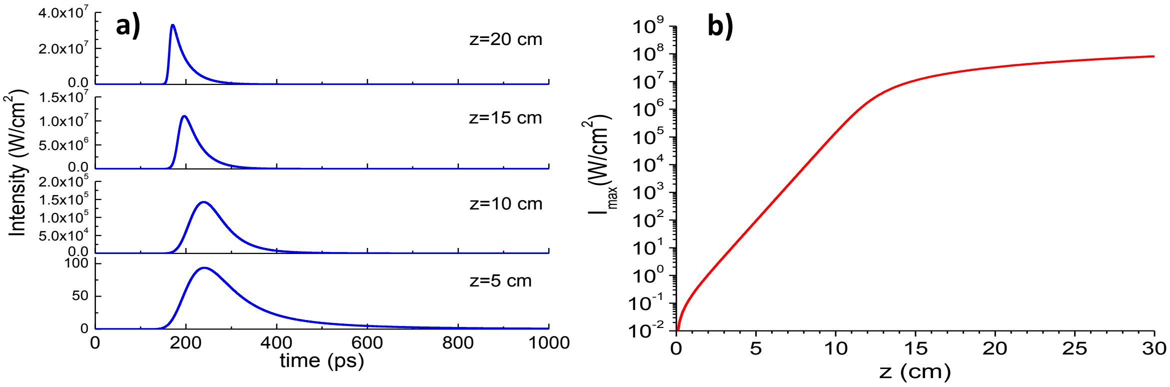

Fig. A5. a) ASE pulse development as a function of filament length. b) Peak intensity in the ASE pulse. The dashed line is the exponential fit with the small signal gain 1.5 cm^{-1}.

Summarizing, we would like to list the main conclusions derived from our model.

- It is possible to achieve population inversion in molecular nitrogen in the afterglow of a femtosecond filament plasma via a cascaded excitation mechanism.
- Electronic temperatures and concentrations, enabling this mechanism, can be achieved in plasma of a femtosecond filament, ignited by a linearly polarized laser radiation. However, this becomes feasible only at long driver wavelengths, 4 μm or longer.
- High plasma density (close to 1 % from air density) is required to outcompete electron recombination and collisional quenching of the excited states.
- Since our model includes negative influence of oxygen as well (the main source of collisional quenching), the results of simulations show that standoff lasing might be achieved under real atmospheric conditions.

As indirect confirmation of our modeling, we refer to the reported last year results in first observations of forward-directed lasing from 4 μm femtosecond filament in pure nitrogen (Fig.A6). All our attempts to observe lasing from pure nitrogen with 1030 nm femtosecond laser system where unsuccessfull, including experiments with circularly polarized light. In contrast, forward directed unpolarized UV emission at 337 nm nitrogen lasing wavelength was clearly observable from 4 μm filament (Fig. A6).

B_ ASE lasing from N2 in air initiated by picosecond optical discharge

B1. Experimental measurements

The theoretical model described in Sec. A incorporates the key aspects of the population dynamics that are well understood in discharge-based N_2 lasers. The derived model provides clear recipes how to overcome difficulties with control over the plasma temperature and concentration in the filament. One needs to provide a source of electron heating within picosecond-sub-nanosecond time scale to reach necessary electronic temperatures and to compensate electron energy losses due to various parasitic inelastic collisions. One such possibility, which is under intense scrutiny today, is the igniter-heater concept. In this concept, the plasma generated by a femtosecond filament is heated by a long (nanosecond) high energy pulse, providing collisional heating of electrons. This concept was investigated numerically and found to be feasible [Henis08, Penãno12]. However, practical realization of this idea is quite difficult because of plasma refraction and coupling of the heater energy into the filament plasma channel. There are no successful reports about realization of this concept so far.

Another possibility, successfully demonstrated by the CROSS TRAP consortium in collaboration with the group of Prof. Polynkin from the University of Arizona, USA, is to extend filamentation into the picosecond pulse range, thereby allowing collisional heating to play a crucial role. This approach, however, sets quite challenging requirements to the laser source that significantly outclasses the sources owned by the Consortium members. That is why we have performed experimental measurements using the Comet laser system which is a part of the Jupiter Laser Facility (JLF) at the Lawrence Livermore National Laboratory [COMET]. The Comet is a Nd glass-based chirped-pulse amplification chain that generates laser pulses at 1,053nm wavelength, with up to 12 J of energy per pulse. The transform-limited output pulse duration is 0.5 ps. The pulses are generated at a rate of one pulse per about five minutes.

The experimental setup is schematically shown in Fig.B1. Collimated beam generated by the Comet laser has a diameter of 90 mm. The beam passes through a 10 mm-thick fused silica exit window of the vacuum compressor chamber of the laser into an about 5m - long gas cell filled with either air or pure nitrogen at the atmospheric pressure. The laser beam is focused by a meniscus lens with a focal length of 2.6 meters. The thickness of the lens at its center is about 3 mm. The pulse energy is varied by changing the pump level in the final amplifier stage. The pulse duration is controlled through tuning the pulse stretcher in the laser system. When varying the pulse energy and duration, the peak pulse power is always kept below ~3.5TW, in order not to generate an excessive nonlinearity in the exit window of the vacuum compressor chamber.

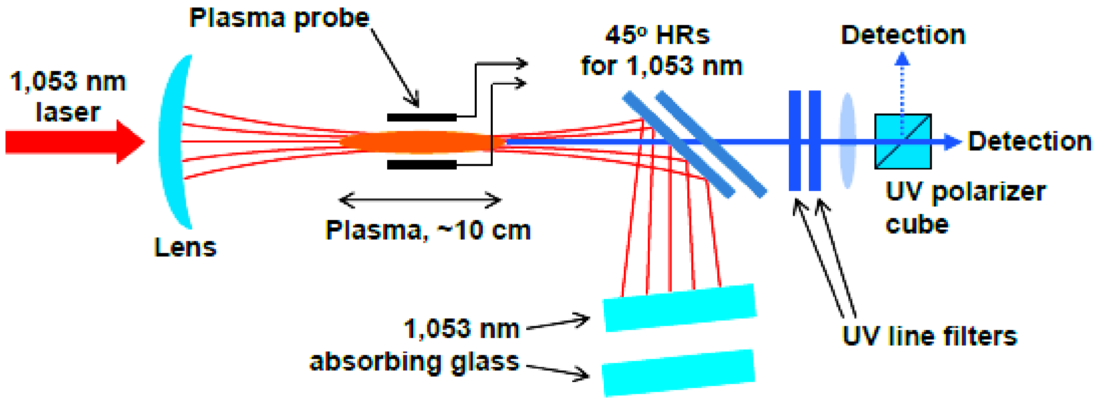

Fig. B1. Schematic of the experimental setup

A weakly focused laser beam creates a plasma channel inside the gas chamber, near the focal plane of the meniscus lens. The length and diameter of the plasma channel are estimated by analyzing photographic single-shot side-images of plasma fluorescence and are found to be about 10 cm and 3 mm, respectively (Fig.B2). For data consistency, plasma density in the channel is monitored, on an arbitrary unit scale, using a capacitive plasma probe described in detail elsewhere [Polynkin12]. In this particular case, the probe has 7 cm×1 cm rectangular electrodes separated by the distance of 2.5 cm and charged to the bias voltage of 50 V. Under these conditions, the peak voltage returned by the probe in response to the plasma generation between the electrodes is of the order of 1 V.

On the detection side, the major part of energy of the diverging pump beam at 1,053nm is reflected by two consecutive 45° dichroic reflectors and absorbed in two 30 mm-thick colored glass plates. The leftover pump light transmitted through the dichroic mirrors is blocked by several interference filters that reject the pump and transmit various UV spectral lines of interest. The transmitted forward-propagating UV light is separated into two polarization components using a polarizer cube. One analyzed polarization is parallel and another perpendicular to the polarization of the pump beam. The UV spectra of both polarizations are recorded by placing the entrance slits of compact spectrometers directly into the beam paths, after the polarization separator. The energy of the UV emission is measured by wavelength-insensitive pyroelectric energy sensors.

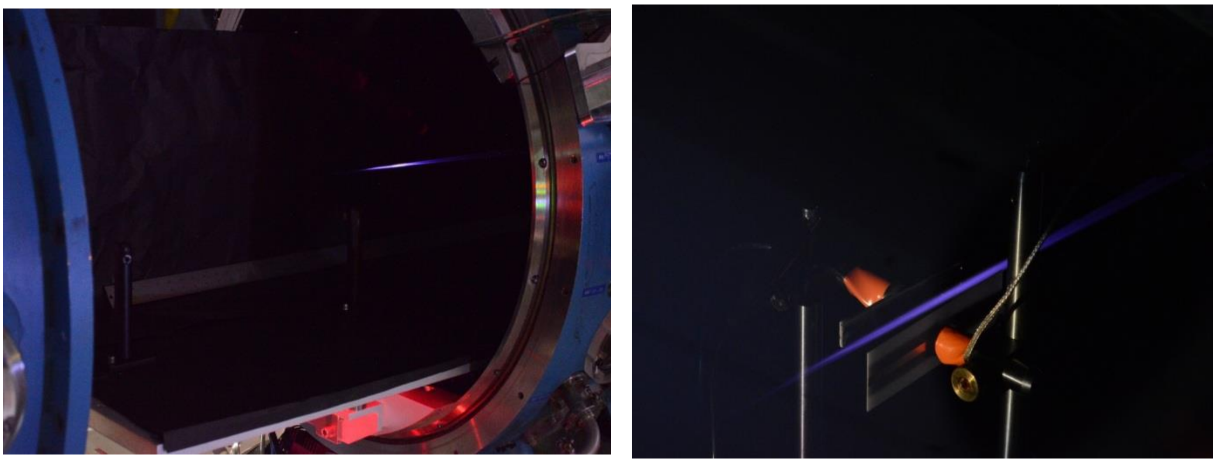

Fig. B2. Left photo - image of a spark in air by a 12 J, 10 ps pulse. Right – close look on plasma channel and plasma density measurements setup.

The examination of the UV part of emission spectrum revealed two dominant features: a broad spectrum at 351nm that corresponds to the third harmonic of the pump beam and the narrow nitrogen emission line at 337 nm. All other UV and visible nitrogen lines, both molecular and ionic, were too weak to be detected. One exception may have been the line at 357 nm. This wavelength is too close to the third harmonic of the pump and might have been obscured. The detectable molecular emission at 337 nm was linearly polarized parallel to the polarization direction of the pump light at 1,053 nm. That suggests that this nitrogen emission was seeded by the short-wavelength spectral tail of the third harmonic of the pump.

An example of the recorded UV part of spectrum is shown in Fig. B3. In this measurement, the pump pulse energy and duration were 10 J and 10 ps, respectively. An interference filter with the bandwidth of 10nm and the center wavelength of 340nm was used to reduce the background from the third harmonic. Even though the third harmonic of the pump is severely attenuated by the filter, it is still the dominant spectral feature, as its total energy is much higher compared to that of the 337nm nitrogen line.

The far-field divergence angle of the third harmonic beam, retrieved from photographs of fluorescence on a paper screen, is about 1°, which is much larger than the diffractive divergence rate corresponding to the mm-scale diameter of the plasma channel inferred from photographic images of the channel. That suggests that the channel is broken up into many individual filaments and the third harmonic beam is highly spatially multimode. The 337nm beam was too weak to be filtered out and imaged separately. However, by translating the spectrometer slit across the beam and recording the amplitude of the 337nm line as a function of the transverse displacement, we found that the divergence of the 337nm beam was also about 1°.

In Figure B4a, we show the amplitude of the 337.1nm line as a function of the peak power of the pump pulse, for three different pump-pulse durations. These power curves show the threshold-like response typical for stimulated emission.

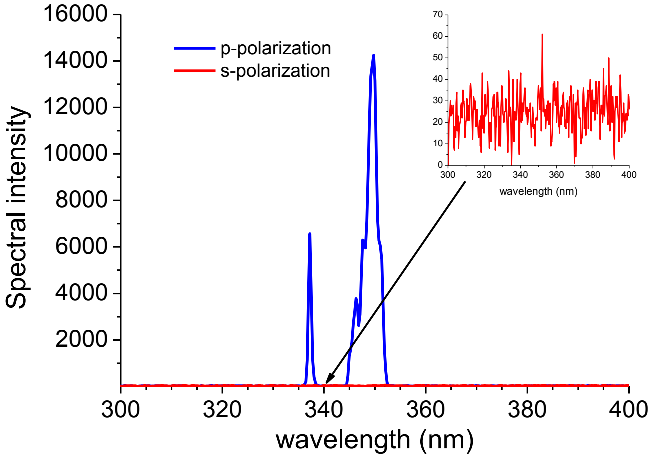

Fig. B3. Measured UV spectrum from the picosecond spark. The inset is spectral measurements in orthogonal polarization.

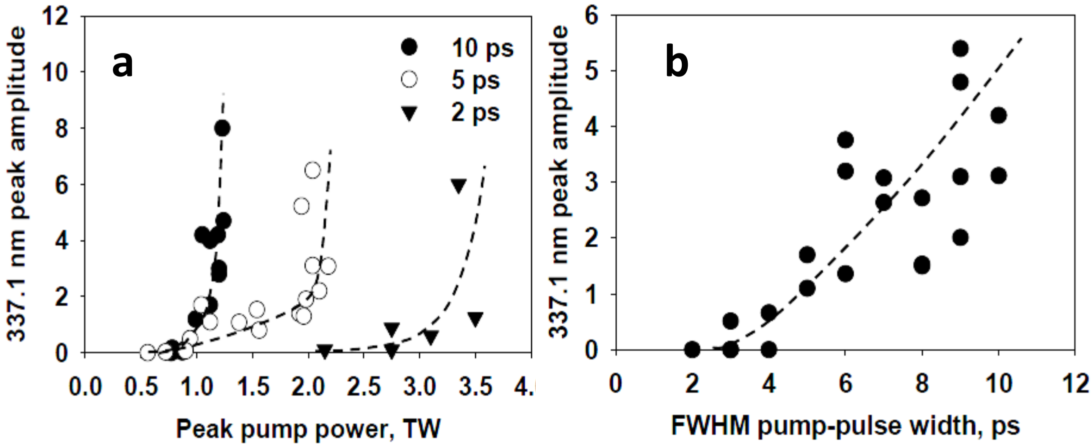

Fig.B4. a) Amplitude of the 337 nm spectral line as a function of the peak power of the 1,053nm pump, for three different durations of the pump pulse. b) Amplitude of the 337nm spectral line as a function of the FWHM width of the pump pulse at 1,053 nm. The peak power of the pump pulse is kept constant at 1.1TW.

In Figure B4b, we show the amplitude of the 337nm line as a function of the FWHM width of the pump pulse. To acquire these data, the duration of the pump pulse and its energy were varied simultaneously while maintaining the peak pulse power constant at 1.1TW. The data suggests that, under our experimental conditions, in order for the population inversion on the 337nm transition to develop, the pump pulse has to be longer than 3 ps. That is consistent with the estimated multi-picosecond-scale time that is needed for the electrons to become sufficiently energetic for inverting the 337nm transition on impact with nitrogen molecules.

The results of time-frequency resolved measurements are shown in Fig.B5. These measurements were carried out with a Hamamatsu streak-camera set at the exit image plane of an imaging polychromator. The time resolution of the streak-camera is about 8 ps. As follows from Fig.B5, the 337 nm emission is indeed seeded by the spectral tail of the third harmonic and delayed in time by about 20 ps.

The total energy emitted in the forward direction in the UV was measured with a pyroelectric energy sensor, using appropriate broadband UV filters. The dominant contribution into the measured energy was from the third harmonic line at 351 nm. The energy in the 337nm line was then evaluated based on the comparison between the relative strengths of the two lines inferred from the emission spectrum. For the case of 10 J, 10 ps pump pulse, which resulted in the strongest 337nm line, the measured energy of the third harmonic at 351nm was 20 mJ, which corresponds to about 0.2% energy conversion from the 1,053nm pump. At that point, the energy in the 337nm line was about 80 μJ.

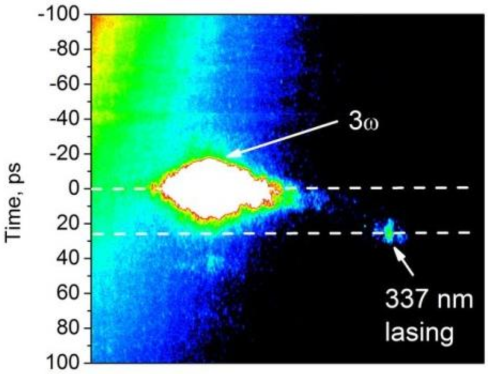

Fig.B5. Streak-camera time-frequency resolved image of the third harmonic and the 337 nm emission. The horizontal axis is uncalibrated frequency axis.

Our measurements allow rough estimation of basic characteristics of the gain medium responsible for the 337nm emission. From the analysis of photographic images of plasma fluorescence, the length and diameter of the gain medium are found to approximately equal 10 cm and 3 mm, respectively. The 337nm emission is seeded by the short-wavelength tail of the third harmonic of the pump. The value of the seed, relative to the amplified signal at 337nm is estimated by extrapolating the short-wavelength spectral tail of the third harmonic line to 337nm wavelength. Assuming that the gain transition is collisionally broadened to about 0.1nm [Papakin85], we estimate the total amplification along the plasma channel as $3 \cdot 10^6$. Ignoring diffraction and other losses and given 10 cm-long active medium, that corresponds to the gain coefficient per unit length of about 1.5 cm^{-1}.

B2. Numerical simulations

Modeling of plasma kinetics in a picosecond optical discharge is much more challenging problem than simulations for the afterglow of a femtosecond filament. Differently from the femtosecond case considered in Part A, when high-energy picosecond laser radiation is focused tightly in gas, the process of optical field ionization is accompanied by electron heating, electron impact ionization and avalanche development. Additionally, electronic excited states in the nitrogen molecule are being significantly distorted by high-intensity laser field that is applied in this case for several picoseconds. Proper description of a picosecond spark would require self-consistent modeling of high intensity picosecond pulse propagation in gas as well as plasma kinetics which includes electron collisional heating, photo and electron impact ionization. To the best of our knowledge, no adequate model has been developed yet. To understand qualitatively the physics of population inversion in a picosecond spark, we have adapted the model developed for femtosecond filaments afterglow with certain modifications explained below.

Under conditions of our experiment, pulse energy 10 J, pulse duration 10 ps, the beam with the diameter 9 cm is focused by a f=2 m lens, the vacuum intensity would exceed 10^{17} W/cm^2. The actual intensity level in the spark is limited by plasma refraction. This intensity can be estimated as follows. When a laser beam with the radius a is focused by a focusing lens with the focal distance f, the critical plasma density balancing the beam convergence is $n^*=n_c\theta^2$ where $\theta=a/f$ and $n_c=10^{21}/\lambda^2$ is the critical plasma density in cm^{-3} for the given laser wavelength λ in μm. For our experiment conditions, this density is $n^*=4.5\cdot10^{17}$ cm^{-3} or about 2% of air density. Using the PPT-model [Perelomov66] with experimentally determined corrections [Talebpour99] to calculate the photo-ionization rate corresponding to a value of 10^{16} W/cm^2 of the vacuum laser peak intensity pessimistically evaluated for the non-Gaussian spatial and temporal profiles of the pump pulse.

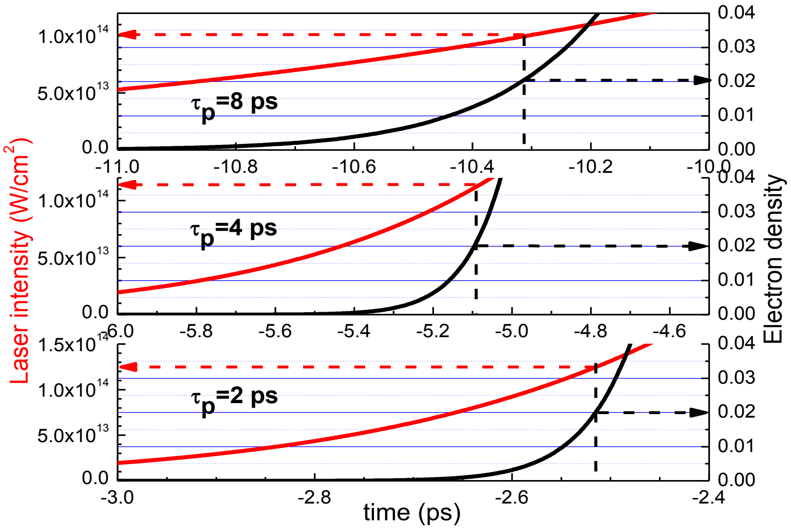

Fig. B6. Time-dependent plasma density from ionized air normalized to the neutral density, for different pulse durations and the peak intensity 10^{16} W/cm^2. The arrows mark the critical density and the corresponding instantaneous pulse intensity.

The calculated time-dependent plasma density determined by photo-ionization only is shown in Fig.B6. As follows from Fig.B6, the critical plasma density is reached on the leading pulse front, well before the pulse peak. It takes about 0.5 ps to reach the critical value, the time scale which is too short for avalanche ionization mechanism to play an important role. Therefore, we assume that the critical plasma density which sets intensity clamping is achieved by the optical field ionization only. From this moment of time laser intensity should decrease rapidly to prevent photoionization and development of the electron avalanche. As follows from our numerical simulations, the intensity ~10^{14} W/cm^2 at the moment of time when strong plasma refraction starts, is pretty high and provides rapid (on the sub-picosecond time scale) collisional heating of electrons, which subsequently triggers an avalanche. Therefore, the intensity should decrease consistently with the plasma density growth to limit the plasma heating and terminate the avalanche. Based on these arguments, we start in our simulations from the pulse intensity $9\cdot10^{13}$ W/cm^2 and the initial plasma density $N_e=2.5\cdot10^{17}$ cm^{-3} corresponding to 1% of the total air density. Then we adapted the model described in section A1, including electron production by photoionization from the ground and excited electronic states in nitrogen and oxygen and electron heating by the laser pulse:

$$\frac{\partial f}{\partial t}=\frac{\partial}{\partial \varepsilon}\left([0.79\delta_1\nu_1(\varepsilon)+0.21\delta_2\nu_2(\varepsilon)]\left(\varepsilon-\frac{4}{3}U_p(t)\right)f\right)+\frac{\partial J_E}{\partial \varepsilon}+\frac{\partial J_{ee}}{\partial \varepsilon}+Q(f)$$
$$+\sum_j W_j f_j^{ph}(\varepsilon) \qquad \text{(B1)}$$

Here $J_E = \frac{8}{3}U_p(t)\nu(\varepsilon)\varepsilon\frac{\partial f}{\partial \varepsilon}$ is the diffusive electron flux over the energy axis due to the laser heating, $U_p(t) = \frac{e^2E^2(t)}{4m\omega^2}$ is the electron pondermotive energy in the laser electric field with the envelope amplitude E(t). The last member in the right side of the equation (B1) describes the source of electrons due to laser filed ionization of molecular oxygen and molecular nitrogen in different electronic states. Here index j enumerates the electronic states in nitrogen or the ground state in oxygen, W_j are photoionization rates calculated with PPT model, functions $f_j^{ph}(\varepsilon)$ are photoelectron energy distribution functions described in details in section A2. During the EEDF evolution, laser intensity decreases exponentially with decrement proportional to the electron density growth.

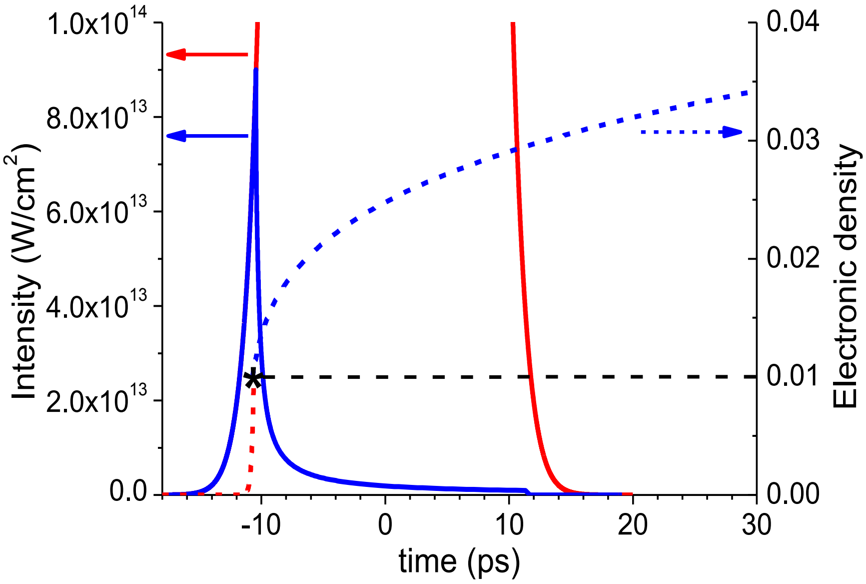

Fig. B7. Red solid line – time profile of the Gaussian laser pulse with FWHM pulse duration 8 ps and peak intensity 10^{16} W/cm^2. The blue solid line shows the actual pulse profile with intensity decay exponentially depending on electron density growth rate. The red dashed line – electron density growth due to optical field ionization. The black star and dashed black line mark the plasma critical density. The blue dashed line shows electron density growth by combined optical field ionization and electron impact ionization. Plasma density is normalized to the neutral density.

Results of simulations for evolution of electronic density and laser pulse intensity in time are presented in Fig. B7. Clearly, plasma density growth due to photoionization occurs on a much shorter time scale than in the avalanche ionization. Also, the intensity decrease on the trailing edge of the pump pulse exponential growth of electron density. The time dependent evolution of electron temperature and population inversion between the lasing B and C states are presented in Fig. B8. High pondermotive energy of electrons (U_p≈10 eV) in the intense laser field at the beginning of plasma evolution determines a remarkably fast collisional heating. The electron temperature grows above 20 eV within less than 1 ps, forming the EEDF similar to that of a hot electron beam (Fig. B9). Then the decrease of the laser intensity reduces electron heating and electrons cool slowly down due to inelastic collisions (Fig. B8,9).

As follows from Fig. B8, population inversion appears about 3 ps after the beginning of the plasma evolution. This result is not sensitive to the rate of intensity decay and matches very well to the experimental observations (see Fig.B4b). The essential condition for the build-up of population inversion is to maintain the duration of the pump pulses longer than 1 ps. However, to seed the nitrogen laser amplifier with a resonant frequency component from the third harmonic spectrum, a pulse duration longer than 3 ps is required, in agreement with our experimental observation. The peak population inversion is expected about 40 ps after the peak of the pulse. This can explain the delay observed in the experiment (Fig.B5).

The mechanism of population inversion, as it follows from our simulations, can be classified as impulsive optical discharge. In a conventional rf or dc discharge, where initial electrons are released by ionization by cosmic rays, it takes about 1 ns to heat electrons, develop avalanche ionization, and reach population inversion. In contrast, impulsive optical discharge in a picosecond spark provides a high initial plasma density via direct optical field ionization. High pondermotive energy acquired by electrons in intense laser field enables very fast electron heating and provides population inversion within several picoseconds time scale. Also, the ultrafast optical discharge allows avoiding negative influence of electron diffusion and heat transfer processes which play crucial role in well-known nanosecond laser sparks.

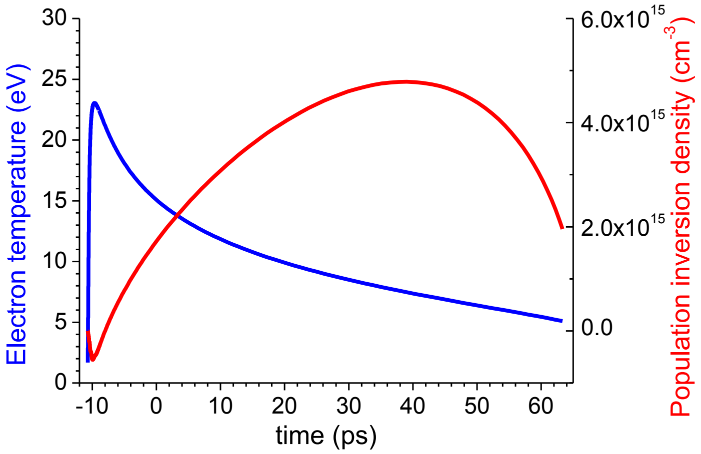

Fig. B8. Blue line – time dependence of the electron temperature. Red line – time dependence of population inversion density.

The results of our modeling suggest a new concept of igniter for standoff atmospheric lasing. In fact, the model hints that picosecond filaments created by high power picosecond laser sources in near-IR spectral range can be very efficient for this purpose rather than femtosecond filaments. Technically, the required picosecond pulse duration can be obtained from CPA and OPCPA setups in which the output pulses carry some residual (under- or over-compensated) chirp.

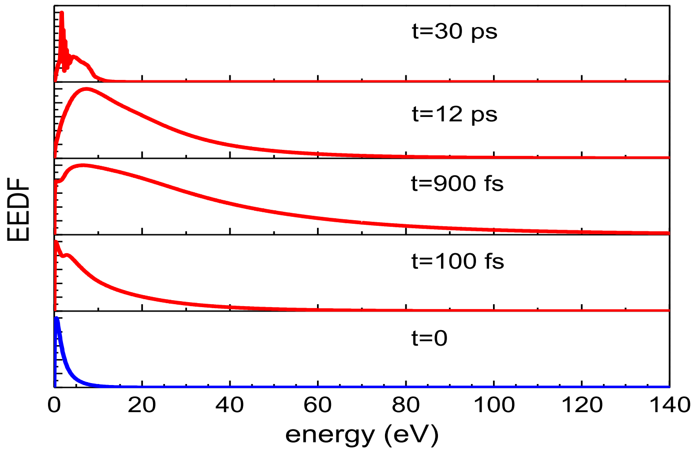

Fig. B9. Time dependent evolution of EEDF.

C_ Directional emission from N_2^+ ions

In the project report for year 2 we demonstrated a new effect of a coherent forward-directed UV emission generation from femtosecond filaments is nitrogen. The UV emission, consisting of very narrow spectral lines at 358, 391 and 428 nm and corresponding to well-known N_2^+ transitions (Fig. C1), was linearly polarized along the laser polarization and was observed from sparks in nitrogen and air ignited by tightly focused femtosecond laser radiation at 4 μm wavelength. Independently, this phenomenon was observed also by the group from China [Yao11] who used tightly focused femtosecond laser radiation at 2 μm wavelength. It is turned out to be a very universal in respect with the wavelength of a high intensity laser creating a spark or a filament in nitrogen, because it was observed also in experiments with two-color spark created by high intensity 800 nm pulse and its second harmonic, as well as in our experiments with femtosecond filamentation in nitrogen by 1030 nm laser pulses. We have shown also that the intensity of this UV emission can be dramatically enhanced when methods of adaptive control over the filamentation pulse are applied and dynamical alignment of nitrogen molecules is induced.

To get insight into physics of this very intriguing phenomenon, we have carried out series of frequency-time-resolved experiments both with single pulse near-IR filaments and with filaments generated by near-IR pulse trains.

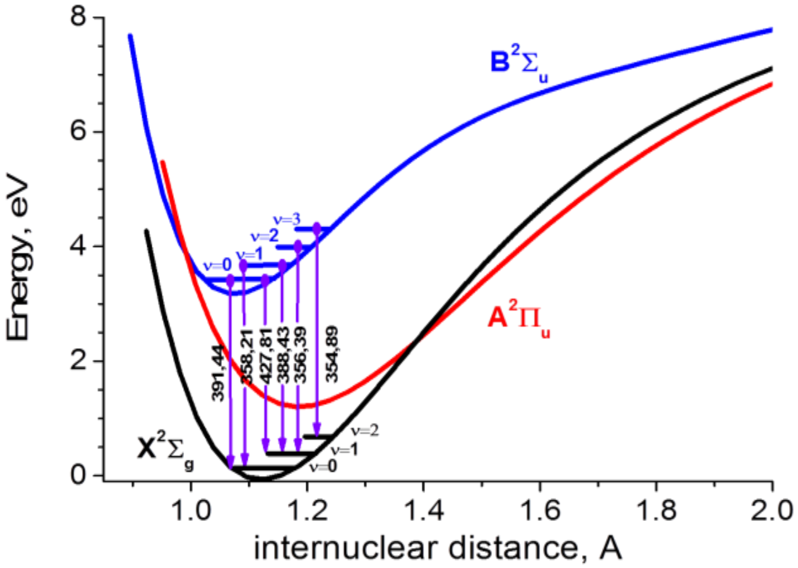

Fig.C1. Diagram of optical transitions in the nitrogen molecular cation.

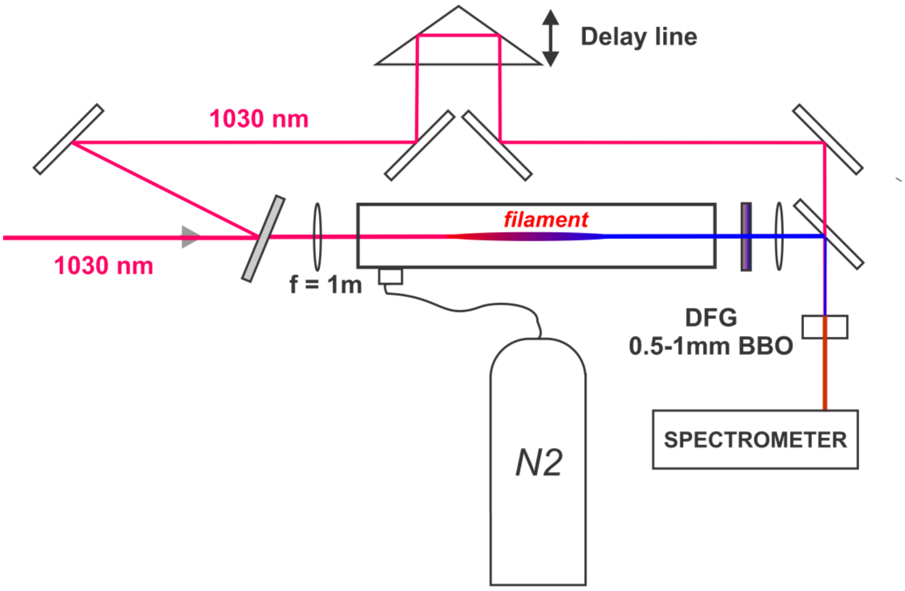

Fig. C2. Experimental setup for time-resolved UV-emission measurements from a single filament.

C1. Time-resolved single-pulse filament measurements

The scheme of the single-filament experimental setup is shown in Fig. C2. Experiments were performed with a home-made kHz repetition rateYb:CaF_2 laser, providing 220 fs, 7 mJ, 1.03 μm pulses [Pugzlys09]. The beam was focused by a *f*=1 m focusing lens into a 1.5-m-long gas cell with transparent sidewalls and Brewster input and output windows made of CaF_2. The cell was pumped below 10^{-1} mbar and filled by pure nitrogen. The small portion of the total energy was split from the main beam before the focusing lens and send to the delay line as a reference beam. The main beam after the cell was collimated by a f=1m silver mirror. For spectral measurements, the collimated beam after the cell was reflected from CaF_2 and quartz wedges and then focused into the optical fiber connected to the spectrometer. For time-resolved measurements we used XFROG setup based on difference-frequency generation (DFG) in a 0.1-0.5 mm thick BBO crystal between the reference beam and the UV part of the output continuum in the vicinity of 391 nm N_2^+ emission line. For XFROG measurements the beam from the cell output was reflected from three broadband dielectric mirrors with high reflection at 400 nm central wavelength and transmitting more than 90% of the fundamental emission at 1030 nm.

It was shown in our early experiments on the coherent UV emission from N_2^+ molecular ion in femtosecond near- or mid-IR filaments that seeding at resonant wavelength is absolutely required for observation of this emission. In mid-IR filaments this seed is provided by high harmonics of the fundamental wavelength (9th and 11th harmonics for 428 nm and 391 nm emission lines correspondingly). The necessity of seeding was confirmed also by the group from SIOM, China working on this problem as well [Yao11. Yao13]. In near-IR filaments, the seed is provided by supercontinuum generation in the vicinity of the third harmonic. In the experiment sketched in Fig. C2 we were changing gas pressure in the cell to control the spectrum broadening and continuum generation in the filament. The optimal pressure for the UV emission generation was 1.8 bar. The corresponding continuum and the UV emission spectrum are shown in Fig. C3.

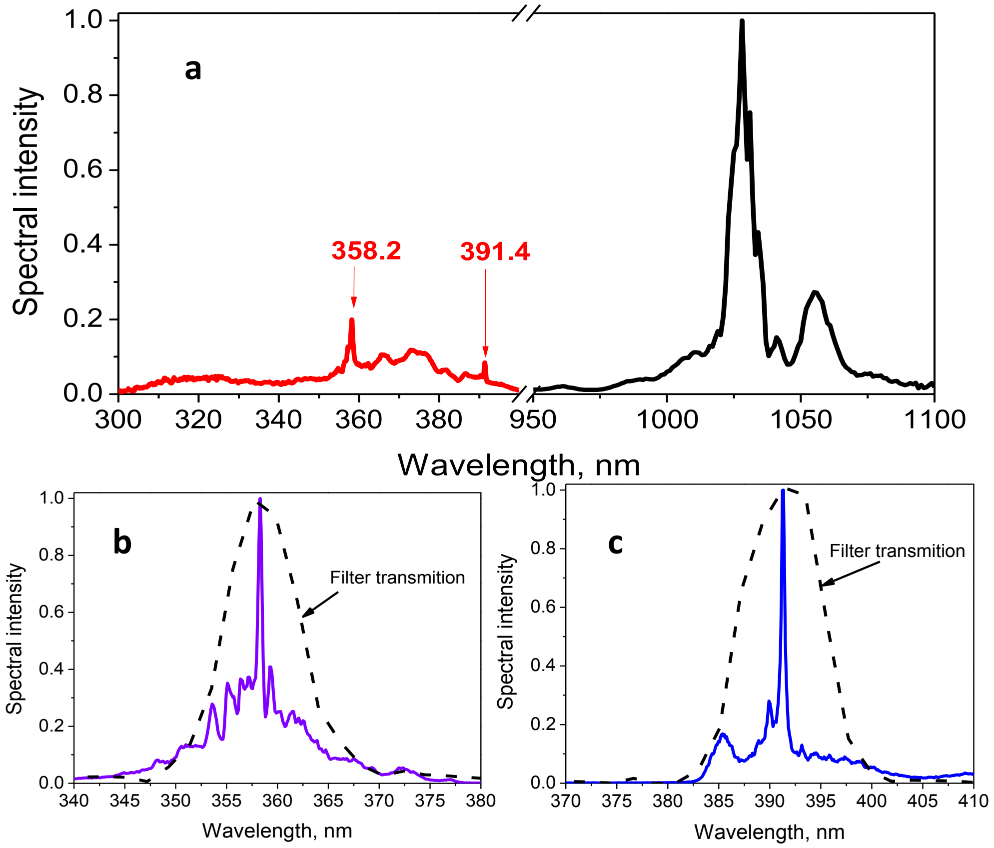

Fig. C3. a) Spectrum from the filament in 1.8 bar nitrogen. b) Spectrum of the 358 nm emission. The dotted line shows the interference filter transmission curve. c) Spectrum of the 391 nm emission.

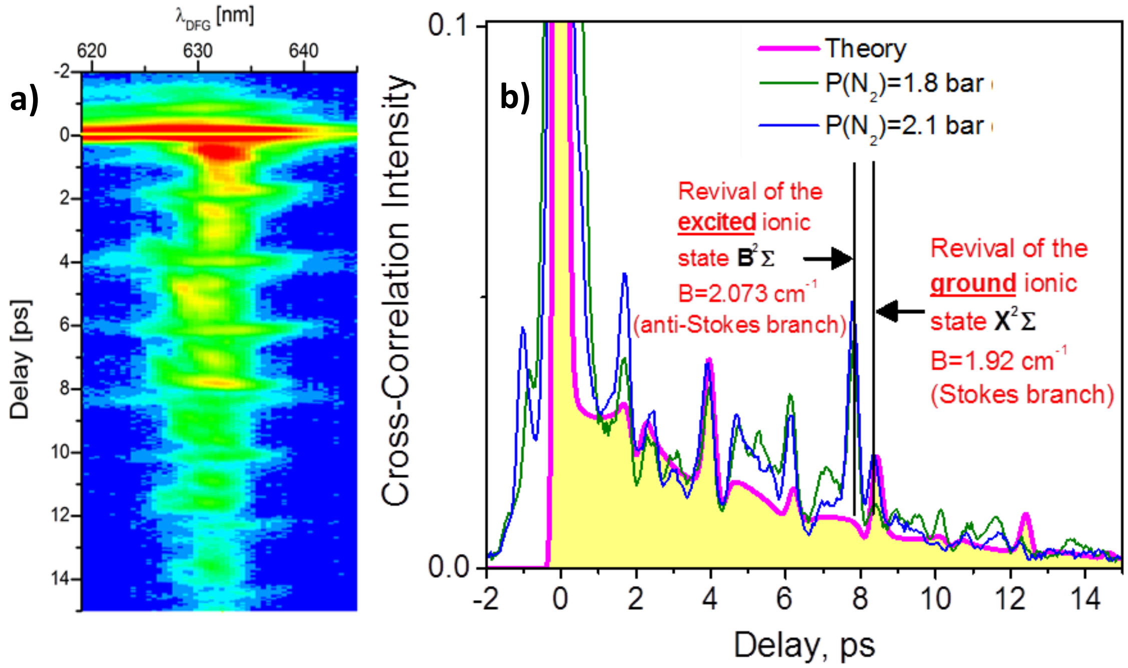

Fig. C4. a) Experimentally measured DFG XFROG trace between 1030 nm reference femtosecond pulse and output continuum in the vicinity of 391 nm wavelength. b) Cross-correlation function retrieved from the XFROG trace. The blue and green lines show the cross-correlation for two different gas pressures. The magenta line shows the results of simulations with FWM with non-instantaneous cubic nonlinearity.

Although the behavior of the observed emission resembles that of a laser-like amplifier, the time-resolved data prove that the coherent UV emission decays over many picoseconds, well outside the temporal overlap with the resonant field of the supercontinuum pulse (Fig. C4). The emitted signal is strongly modulated in time with the periodicities corresponding to the rotational revivals of both the ground and the excited ionic states, whereas its carrier frequency is modulated by the rotational revivals of neutral nitrogen molecules and is consistent with description given in [Ripoche97]. This complex ringing tail structure provides a strong hint about the importance of rotational excitations in N_2^+ and suggests the first possible candidate for the explanation of the physical mechanism behind this emission. This is the four-wave-mixing (FWM) scenario on non-instantaneous cubic nonlinearity in rovibrationally excited molecules. This scenario is sketched in Fig. C5 and the basic principles are explained in details in the monograph [Mukamel]. The suggested FWM process involves two successive interactions with a high-intensity non-resonant near-IR field, one of the roles of which, beside the generation of ions, is the excitation of their rotational Raman manifold. Subsequent interaction with a weak resonant UV field leads to an automatically phase-matched emission of intense 3rd order polarization at Stokes and anti-Stokes frequencies around the resonance:

$$P^{(3)}(t)=\int_0^\infty dt_3\int_0^\infty dt_2\int_0^\infty dt_1 E_3(t-t_3)E_2(t-t_3-t_2)E_1^*(t-t_3-t_2-t_1)S^{(3)}(t_3,t_2,t_1)$$

where

$$S^{(3)}(t_3,t_2,t_1)=\left(\frac{i}{\hbar}\right)^3\theta(t_3)\theta(t_2)\theta(t_1)\sum_{\alpha=1}^{4}R_\alpha(t_3,t_2,t_1)$$

, $\theta(t_i)$ is Heaviside function and $R_\alpha(t_1,t_2,t_3)$ is the molecular time-domain response function which is the Fourier transform from the frequency- dependent susceptibility measured in [Ripoche97]. The results of simulations are shown as a magenta line in Fig.C4. Clearly, the model of FWM on non-instantaneous cubic nonlinearity does not describe well all features in the complex XFROG trace measured in the experiment.

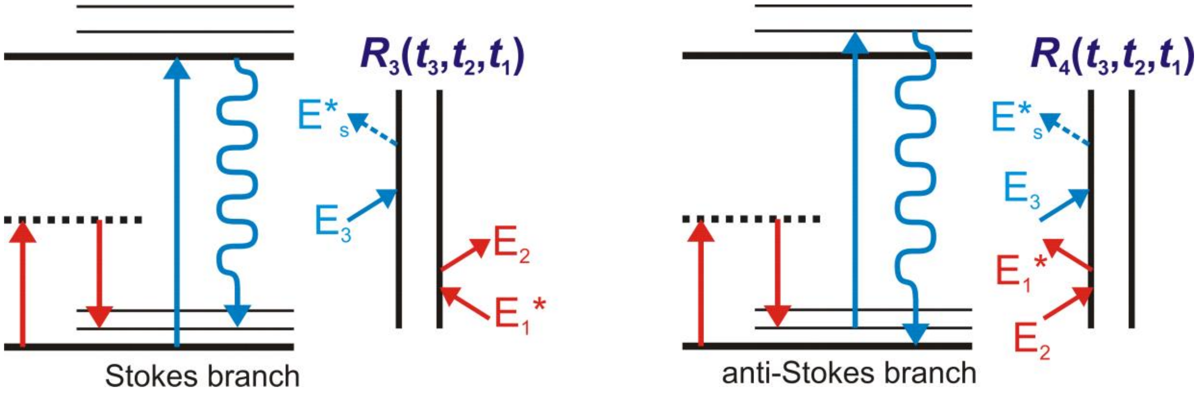

Fig. C5. FWM diagrams. Thick lines indicate vibrational levels of $X^2\Sigma_g$ and $B^2\Sigma_u$, thin lines represent rotational levels. The spectrum of nearly transform-limited near-IR pulses is sufficiently broad for Raman-type excitation of the rotational manifold.

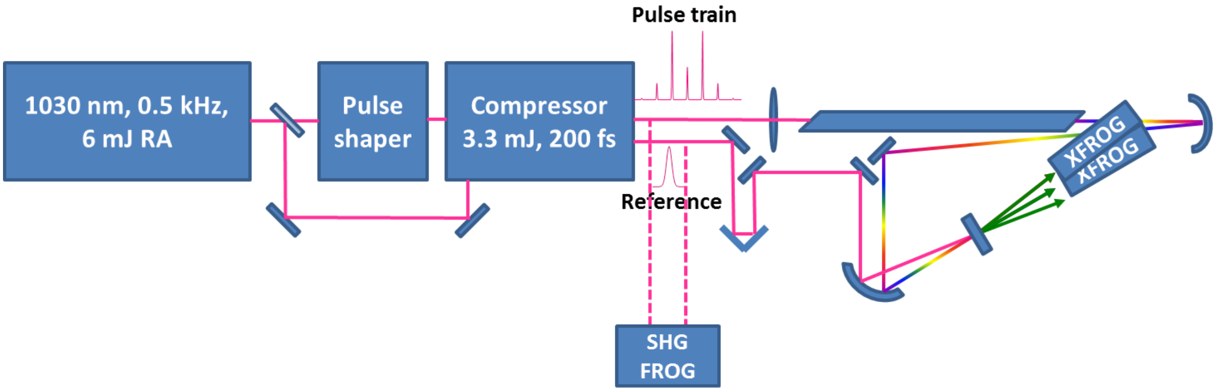

Fig. C6. Experimental setup for time-resolved measurements of filamentation with adaptive control.

Our time-resolved measurements of the coherent UV emission from single pulse filaments demonstrate that rotational molecular dynamics plays crucial role in the process of emission.

C2. Time-resolved measurements for filaments generated by adaptively controlled pulse trains.

To understand the role of molecular rotations in the process of the coherent UV emission from nitrogen molecular cation in femtosecond filaments, we have carried out time-resolved experiments with filaments generated by adaptive controlled pulse trains. This is for the first time, to the best of our knowledge, application of adaptive control over the efficiency of UV emission from nitrogen in a near-IR femtosecond filament using a spatial light-modulator (SLM).

The pulse shaper, comprising an SLM in a 4*f* fold of cylindrical mirrors, was installed after the regenerative amplifier, before the compressor (Fig. C6). As a reference pulse for DFG XFROG measurements, we used the zero-order diffraction beam from the first grating in the shaper. The reference pulse and the beam from the shaper output where send in parallel in the same compressor. The total throughput efficiency of the shaper and compressor was measured 65%, resulting in about 4 mJ energy in the shaped pulse. The pulse after shaper was focused then with a f=1m focusing lens into the 1.5-m-long gas cell used before in the single pulse experiments. The compressor was adjusted to optimize temporal structure of the reference pulse. The residual chirp in the pulse from the pulse shaper, originating from difference between the gratings in the shaper and in the compressor, was compensated by the optimization phase applied to the SLM. To determine this optimal phase, we characterized the pulse after the shaper with SHG FROG measurements. Then a genetic algorithm was applied to compensate high order phase distortions. The optimized reference and shaper pulses are shown in Fig. C7.

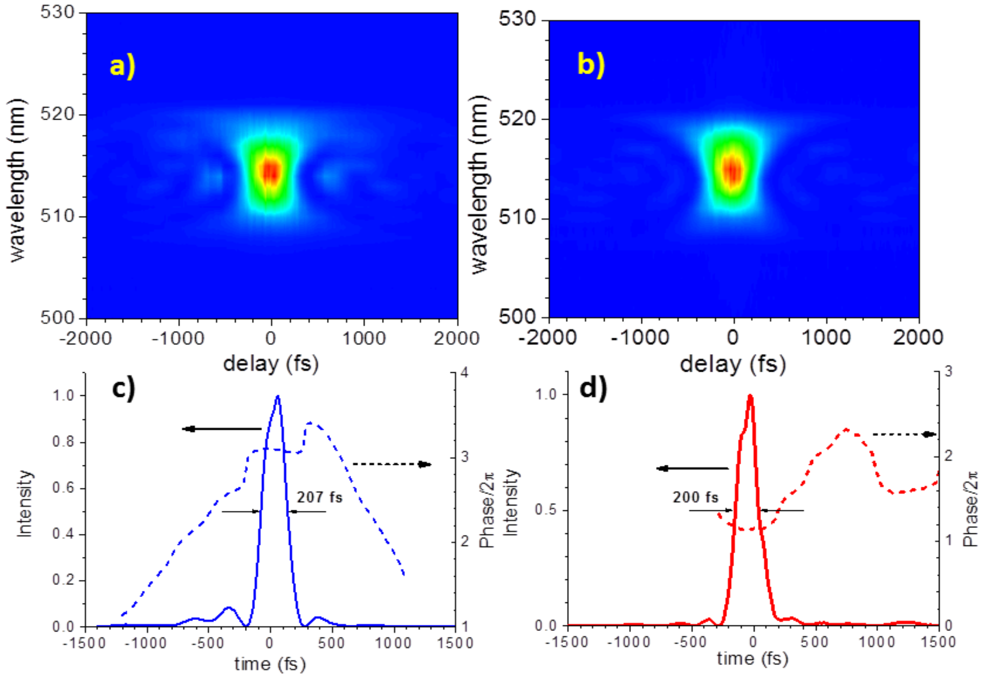

Fig. C7. a) Measured SHG FROG trace and c) reconstructed reference pulse; b) measured SHG FROG trace and d) reconstructed pulse after the shaper with optimal phase mask.

To control molecular alignment in the filament, we have used a class of sinusoidal masks φ(ω)=*a* sin(*b*ω+*c*) to the spectral phase of the compressed laser pulse, where the parameter *a* determines the relative amplitudes and the number of pulse replicas and *b* the temporal delay between them (Fig. C8) [Zeidler01]. The parameter *c* was set to 0 for the central wavelength 1030 nm in the pulse spectrum.

To define the optimal set of parameters for the highest efficiency of the 391 nm emission, we performed three-parametric scan varying the pulse separation in the train (parameter *b*), phase mask amplitude (parameter a) and gas pressure. The optimal gas pressure is defined by the pulse energy and the peak power available in the experiment. The main role of the gas pressure, we believe, is the optimization of the efficiency and spatio-temporal structure of supercontinuum generation in the pulse train. Since resonant seed is one of the necessary conditions to observe the effect, sufficient spectral broadening in the vicinity of the third harmonic with a spatial structure well-overlapped with the plasma channel are required. Taking into account that the maximum available in the experiment pulse energy is divided up over several sub-pulses, the optimal nitrogen pressure was found to be about 5 bars. For lower pressure, the efficiency of white light generation decreases rapidly. On the end of the optimal range, at substantially higher pressures the onset of multiple filaments sets the limit for the coherent UV emission generation. We believe that with shorter pulses in the train and higher laser system output energy the results presented here could be obtained under normal pressure conditions.

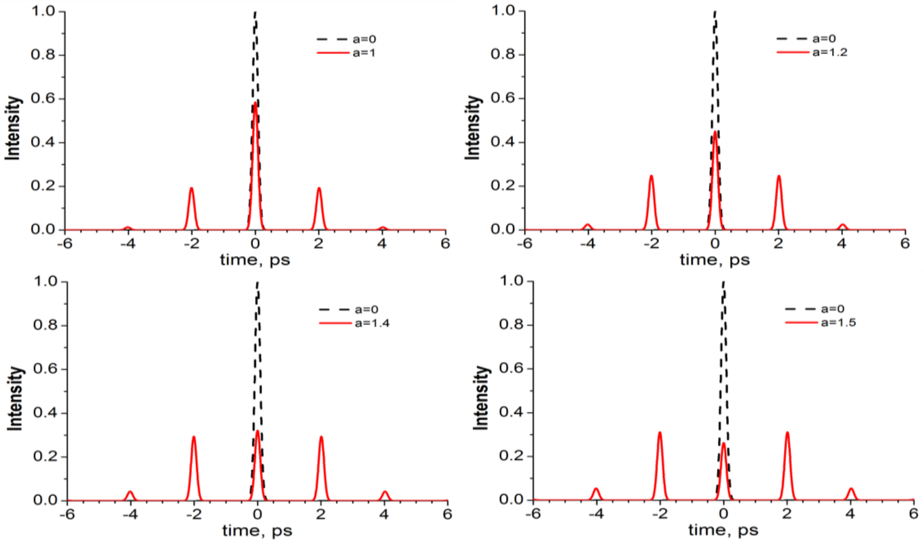

Fig. C8. Pulse sequence generated by the SLM for different values of the parameter a and the delay b=2ps.

The optimal phase mask amplitude was found to be *a*≈1.9. This optimal value is related to the optimal energy partition between the pulses in the train and will be discussed further.

The results of spectral measurements as a function of the pulse separation for the optimal value of the *a*-parameter are shown in Fig.C9. These measurements were performed with the 10nm bandwidth, 400 nm transmission wavelength interference filter to avoid spectrometer saturation by the rest of the spectral supercontinuum. Clearly, under optimal conditions the 391 nm emission is much more intense than the supercontinuum generated in this spectral region (Fig. C9b). As follows from Fig. C9c, the optimal pulse delay is *b*=2126 fs and it should be adjusted with a remarkably high accuracy of ± 15 fs. Precise tuning of a delay between the pulses is required not only to observe the 391 nm narrow band emission, but also to observe white light continuum generation from the filament. This result is consistent with [Varma08, Varma12] and confirms that molecular quantum wake provides ultrafast modulation of nonlinearity in the medium.

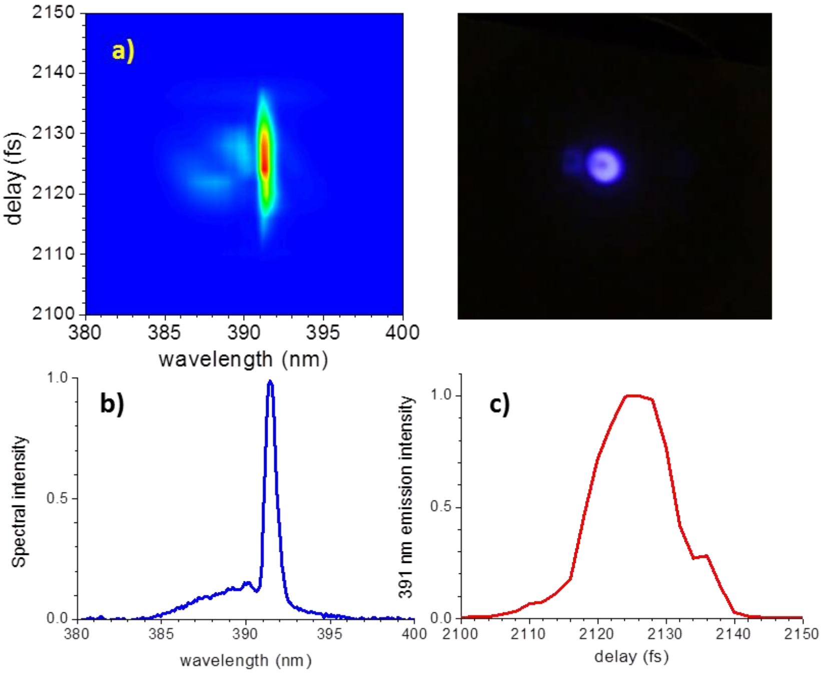

Fig. C9. a) 2D map of the UV spectrum as a function of delay between the pulses in the train. b) Integrated over all delays 2D distribution from a) provides the generated UV spectrum. c) Integrated over all wavelengths 2D distribution from a) provides the dependence of 391 nm emission on the delay between the pulses. The resolution in delay is 2 fs. The photo shows the spatial structure of the generated 391 nm emission.

For time-resolved measurements the XFROG setup with 500 μm thick I-type BBO crystal was used. To reveal the role of individual pulses in the train for the 391 nm emission generation, we have measured the SFG XFROG traces for the reference 1030 nm beam with the 1030 nm pulse train after the cell and the DFG XFROG traces with the part of the spectrum in the beam after the cell in the vicinity of 391 nm wavelength. To make these measurements with absolute relative delay calibration, we were rotating the reference pulse polarization by a half-wave plate and the nonlinear crystal by 90°, since the SFG XFROG requires the type I interaction and the DFG XFROG requires the type II interaction with reference beam polarization perpendicular to the polarization of 391 nm emission. The results of measurements for the optimal pulse train are presented in Fig. C10. The time axis direction in Fig. C10 was determined from comparison of the SFG XFROG measurements of the train passing the cell under vacuum and under 5 bars of nitrogen. In 2D XFROG map, the train propagated through the vacuum cell is shifted by about 8 ps to the right. Therefore, the right side in Fig. C10 corresponds to the earlier moments in time, which is reflected in the numeration of the pulses in the simulated train (Fig. C10a). As follows from Fig. C10c,d, the two most intense pulses in the train marked as (2) and (4) play the major role for 391 nm emission, which is generated with a delay about 0.9 ps after the (4) pulse. The comparative plot of cross-correlation functions, clearly demonstrating this delay, is shown in Fig. C11. In calculation of this delay we took into account the delay about 500 fs between 1030 nm and 391 nm colors after their propagation in the 2 mm thick Brewster output window and about 3 m of air from the cell till the nonlinear crystal.

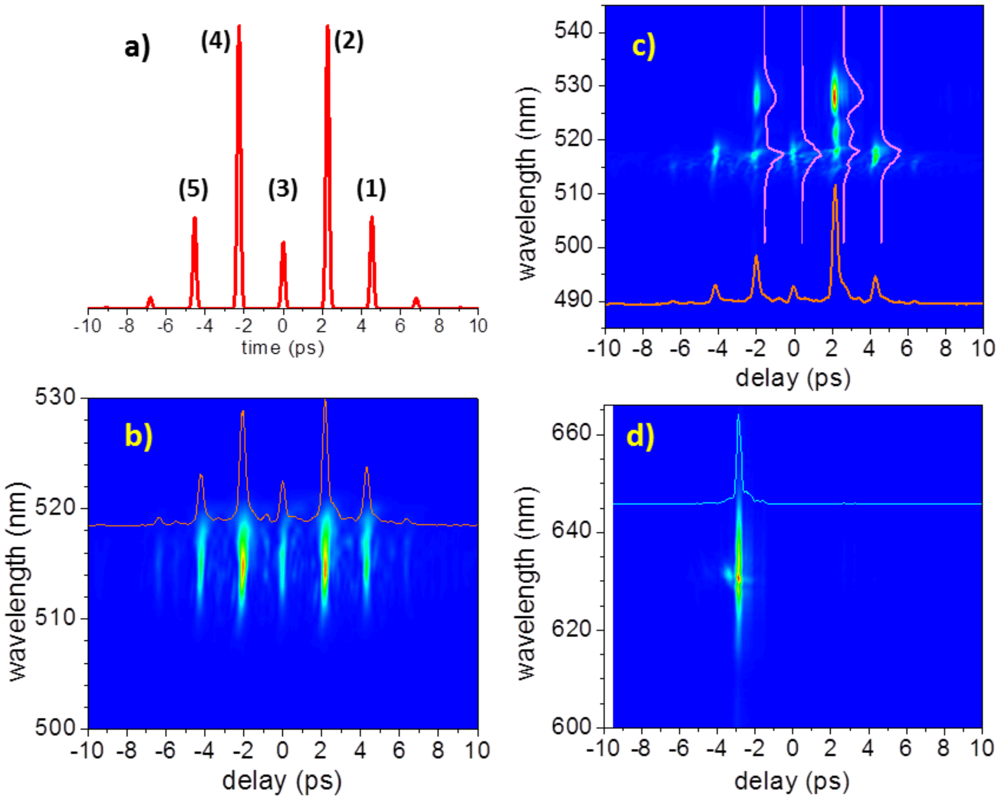

Fig. C10. a) Simulated optimal pulse train with a=1.9, b=2130 fs; b) SFG XFROG trace and cross-correlation between the reference pulse and the optimal pulse train after the cell pumped below 10^{-2} *mbar; c) SFG XFROG trace and cross-correlation with the optimal pulse train after the cell filled by nitrogen under 5 bars pressure. The light magenta lines show the spectra of each individual pulse in the train; d) DFG XFROG trace and cross-correlation with the part of white light having spectrum in the vicinity of 391 nm.*

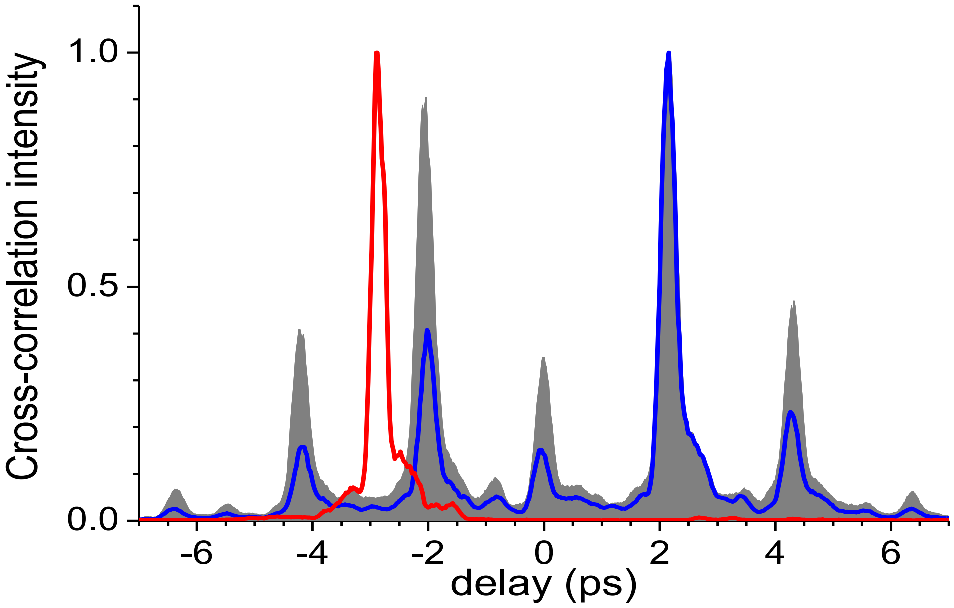

Fig. C11. Gray shaded plot – cross-correlation from SFG XFROG trace between the reference pulse and the optimal pulse train propagating through the cell under vacuum; blue line – the same for the train propagating through the cell filled by nitrogen under 5 bars pressure; red line - cross-correlation from DFG XFROG trace between the reference pulse and 391 nm emission.

The time-frequency-resolved measurements allow us to assign the roles of each individual pulse in the train. Pulse (2) creates the primary filament and induces strong impulsive alignment in molecular nitrogen. Pulse (4), appropriately delayed with respect to pulse (2), creates the secondary filament and generates white light due to enhanced nonlinearity induced by molecular alignment. This white light serves as a seed for X-B transition in the molecular nitrogen ion (see Fig.C1). This scenario explains the structure of the optimal pulse train. For the phase mask amplitude *a*=1.9 peak power in the (2) and (4) pulses is maximal, providing the strongest control effect. For lower mask amplitudes, the growth of the central peak intensity leads to suppression of the pulses. For higher mask amplitudes, the same effect is caused by the growth of peaks (1) and (5) and appearance of more pulses in the train.

A very interesting observation from the time-resolved measurements is that the initial equidistant pulse separation 2126 fs, set by the pulse shaper and confirmed by peak-to-peak measurements of cross-correlation for the pulse train propagating through the vacuum cell, has changed under nonlinear propagation in the gas. The actual time delay between the (2) and (4) pulses became 4172 fs (instead of 4244), close to the half-revival time for the rotational wavepacket in the ground state of neutral nitrogen molecule. This result suggests linear and nonlinear change in the group velocity of sequential pulses in the train induced by ultrafast modulation of optical properties of the medium.

The conclusive physical picture of the observed coherent UV emission from the molecular nitrogen ion in femtosecond filaments is not developed yet. More detail investigations are required to identify the physical mechanisms behind this phenomenon. As mentioned before, one of the striking features of this process is its universality – it was observed under very different experimental conditions with very different femtosecond laser sources. Currently we consider two possible explanations.

The first explanation was proposed in [Yao11] and assumes that a laser-like mechanism of stimulated amplification of the resonant seed generated in the filament is responsible for the observed effect. Strong supporting argument for this hypothesis is an experimental evidence of amplification of an external resonant seed light coupled into the filament/spark. Such externally seeded amplification was reported for two-color experiments with 800 nm femtosecond pulses and the second harmonic 400 nm seed, co-propagating and contra-propagating with the main pulse and for both cases of parallel and orthogonal polarizations [Yao13, Ni13]. Also, similar measurements were reported in [Yao11] where the spark was ignited by a tightly focused 1.9 μm femtosecond laser beam and the seed was the second harmonic of a 800 nm femtosecond source. However, a physical mechanism which would provide population inversion in N_2^+ is absolutely not clear. Also, all attempts to seed resonantly the filaments generated in our experiments by 1.03 and 3.9-μm pulses resulted in the observation of strong absorption of the seed light at 391 nm wavelength. Our experimental measurements as well as the cited published works show that the UV emission is generated within a very short time. It is known that multiphoton or tunnel ionization of neutral nitrogen molecule in the ground electronic state creates molecular ion also in the ground state. On this femtosecond – picosecond time scale the X-B system in N_2^+ can be considered as a two-level system, where population inversion is possible neither by one-photon, nor by multi-photon excitation.

The second explanation was proposed recently by our collaborator Prof. Misha Ivanov from Max Born Institute, Germany. He suggested a very interesting idea of a molecular laser amplifier without inversion, which shown to be feasible in our simulations. This scenario can be best explained for the conditions of our experiments with adaptive pulse control. Pulse (2) in the train induces molecular alignment in the neutral nitrogen and, as a result, in the molecular ion as well. The role of pulse (4) is to make populations in the ground and the excited B-state of N_2^+ comparable (but not inverted!) via single photon excitation. This can be achieved relatively easily due to the large corresponding transition dipole moment [Lofthus77]. The excitation leads to the formation of a rotational wave packet in the excited B-state as well. Due to mismatch in the rotational constants (1.92 and 2.073 cm^{-1}, resulting in 8.687 ps and 8.045 ps full revival time for the ground and the B-state respectively), the rotational wavepackets in the ground state and in the excited B-state loose synchronization quite rapidly (Fig. C12). Since the X-B excitation is a parallel transition, the absorption probability for the resonant 391 nm quanta is defined by the amount N_X of molecules in the ground X-state aligned along the laser polarization: $W_{X\text{->}B} \sim \langle\cos^2\theta\rangle_X N_X$. Similarly, the probability of emission is defined by the amount of aligned molecules in the B-state: $W_{B\to X} \sim \langle\cos^2\theta\rangle_B N_B$. Introducing the ratio $R=N_B/N_X$, we can express the difference between the absorption and the emission probabilities as $\Delta W \propto \{\cos^2\theta\}_X (t) - R\cdot\{\cos^2\theta\}_B (t)$. The time dependence of this value, characterizing the gain and retrieved from quantum-mechanical simulations of rotational molecular dynamics, is presented in Fig.C13. As follows from Fig.C13, there are narrow time windows when amplification without population inversion can occur. Note that these simulations do not include a decay of rotational revivals, which for N_2^+ occurs within few tenses of picoseconds [Azarm10].

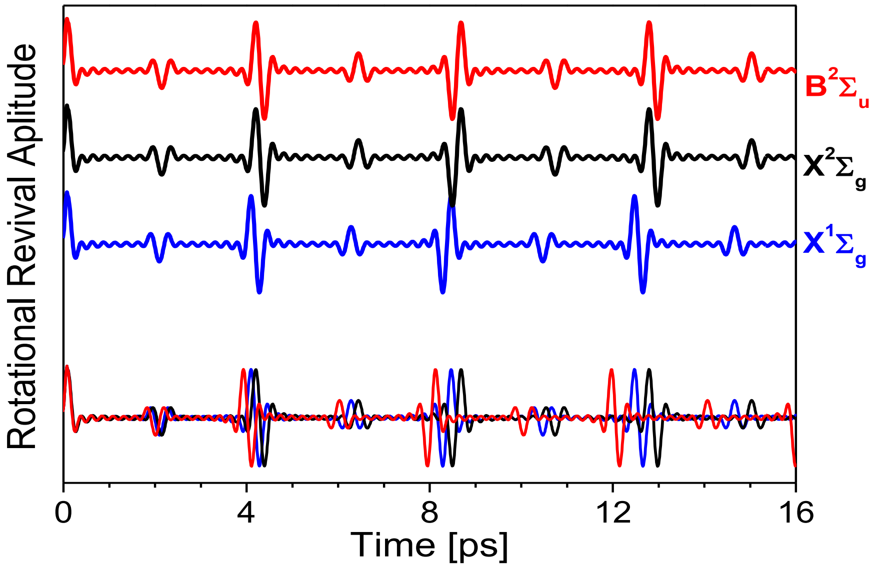

Fig. C12. Rotational revivals for the ground state in neutral nitrogen, the ground state in nitrogen cation and the excited B-state.

The suggested idea of molecular laser amplifier without inversion is quite universal and could be applied to the single pulse experiments as well. The reason is because the ionization probability in molecules depends strongly on molecular orientation in respect to the laser polarization [Pavičić07]. Therefore, an aligned molecular wavepacket is created naturally by photoionization step. Then, the excitation by the seed is also polarization sensitive and makes additional alignment selection of the molecular ions in the excited state. Therefore, conditions of amplification without inversion could be realized under single pulse experimental conditions as well, although the alignment quality in this case is much worse than in experiments with control methods applied.

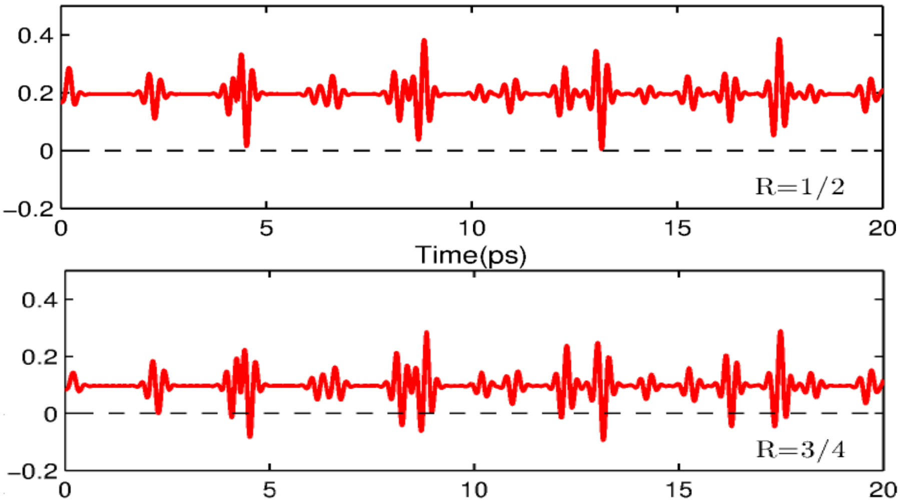

Fig. C13. Upper panel -gain without inversion for R=1/2 (67% population in the ground and 33% in the B-state correspondingly), lower panel - for R=3/4 (57% population in the ground and 43% in the B-state correspondingly).

2_ CONCLUSIONS

In this deliverable:

- We developed an advanced model for nitrogen population dynamics. The model links the photo-ionization (femtosecond time scale) and plasma-chemical dynamics (picosecond—nanosecond time scale) in a self-consistent way.
- We observe delayed picosecond lasing at 337 nm in the experiments with a Joule-class picosecond CPA laser proving that the origin of optical gain is transient population inversion.
- The results of the observed 337-nm lasing are corroborated by our numerical modeling.
- We identify a novel mechanism of laser amplification which is based on periodic rotational revivals of the ground and excited states of N_2^+ and does not require population inversion. The temporal structure of this amplification is resolved in the latest time-gated experiments presented in the report.

3_ REFERENCES

[Azarm10] A. Azarm, S. Ramakrishna, A. Talebpour, S. Hosseini, Y. Teranishi, H. L. Xu, Y. Kamali, J. Bernhardt, S. H. Lin, T. Seideman, S. L. Chin, "Population trapping and rotational revival of N_2 molecules during filamentation of a femtosecond laser pulse in air", Journ. Phys. B 43, 235602 (2010).

[Bacri82] J. Bacri and A. Medani, "Electron diatomic molecule weighted total cross section calculation. III Main inelastic processes for N_2 and N_2^+", Physica C 112, 101 (1982).

[Bodrov11] S. Bodrov, V. Bukin, M. Tsarev, A. Murzanev, S. Garnov, N. Aleksandrov, A. Stepanov, "Plasma filament investigation by transverse optical interferometry and terahertz scattering", Opt. Express 19, 6829 (2011).

[COMET] Jupiter Laser Facility at Lawrence Livermore National Laboratory: https://jlf.llnl.gov.

[Couairon07] A. Couairon, A. Mysyrowicz, "Femtosecond filamentation in transparent media", Phys. Rep. 441, 47 (2007).

[Hunter81] A. M. Hunter, R. 0. Hunter, "Bidirectional Amplification with Nonsaturable Absorption and Amplified Spontaneous Emission", IEEE Journ. Quant. Electr, QE-17, 1879 (1981).

[Haag83] G. Haag, M. Munz, G. Marowsky, "Amplified Spontaneous Emission (ASE) in Laser Oscillators and Amplifiers", IEEE Journ. Quant. Electr, QE-19, 1149 (1983).

[Henis08] Z. Henis, G. Milikh, K. Papadopoulos, A. Zigler, J. Appl. Phys. 103, 103111 (2008).

[Pavičić07] D. Pavičić, K. F. Lee, D. M. Rayner, P. B. Corkum, and D. M. Villeneuve, Phys. Rev. Lett. 98, 243001 (2007).

[Itikawa06] Y. Itikawa, "Cross Sections for Electron Collisions with Nitrogen Molecules", Journ. Phys. Chem. Ref. Data 35, 31 (2006).

[Itikawa09] Y. Itikawa, "Cross Sections for Electron Collisions with Oxygen Molecules", Journ. Phys. Chem. Ref. Data 38, 1 (2009).

[Kossyi92] I A Kossyi, A Yu Kostinsky, A A Matveyev, V P Silakov "Kinetic scheme of the nonequlibrium discharge in nitrogen oxygen mixtures", Plasm. Sour. Science Tech. 1, 207 (1992).

[Kunabenchi84] R. S. Kunabenchi, M. R. Gorbal, and M. I. Savadatti, "Nitrogen lasers", Prog. Quant. Electr. 9, 259 (1984).

[Lin98] J.Y. Lin, G.J. Tallents, J. Zhang, A.G. MacPhee, C.L.S. Lewis, D. Neely, J. Nilsen, G.J. Pert, R.M.N. O'Rourke, R. Smith, E. Wolfrum, "Gain saturation of the Ni-like X-ray lasers", Opt. Commun. 158, 55 (1998).

[Lin99] J.Y. Lin, G.J. Tallents, A.G. MacPhee, A. Demir, C.L.S. Lewis, R.M.N. O'Rourke, G.J. Pert, D. Ros, P. Zeitoun, "Travelling wave chirped pulse amplified transient pumping for collisional excitation lasers", Opt. Commun. 166, 211 (1999).

[Lofthus77] A. Lofthus, P.H. Krupenie, "Spectrum of molecular nitrogen", Journ. Phys. Chem. Ref. Data 6, 113 (1977).

[Papakin85] V. F. Papakin, A. Yu. Sonin, "Measurement of the gain of an ultraviolet nitrogen laser", Sov. J. Quant. Electr. 15, 581 (1985).

[Penãno12] J. Penãno, P. Sprangle, B. Hafizi, D. Gordon, R. Femsler, M. Scully, J. Appl. Phys. 111, 033105 (2012).

[Mukamel] S. Mukamel, "Principles of Nonlinear Optical Spectroscopy", Oxford University Press (1999).

[Mur01] V. D. Mura, S. V. Popruzhenko, V. S. Popov, "Energy and Momentum Spectra of Photoelectrons under Conditions of Ionization by Strong Laser Radiation (the Case of Elliptic Polarization)", JETP 92, 777 (2001).

[Ni13] J. L. Ni, W. Chu, C. R. Jing, H. S. Zhang, B. Zeng, J. P. Yao, G. H. Li, H. Q. Xie, C. J. Zhang, H. L. Xu, S. L. Chin, Y. Cheng, Z. Z. Xu, "Identification of the physical mechanism of generation of coherent N-2(+) emissions in air by femtosecond laser excitation", Opt. Express 21, 8746 (2013).

[Perelomov66] A. M. Perelomov, V. S. Popov, and M. V. Terent'ev, "Ionization of atoms in an alternating electric fields", Sov. Phys. JETP **23**, 924 (1966) [Zh. Eksp. Teor. Fiz. 50, 1393 (1966)].

[Polynkin12] P. Polynkin,"Mobilities of O_2^+ and O_2^- ions in femtosecond laser filaments in air", Appl. Phys. Lett. 101, 164102 (2012).

[Pugzlys09] A. Pugžlys, G. Andriukaitis, A. Baltuška, L. Su, J. Xu, H. Li, R. Li, W.J. Lai, P.B. Phua, A. Marcinkevičius, M.E. Fermann, L. Giniūnas, R. Danielius, and S.

Ališauskas, “Multi-mJ, 200-fs, cw-pumped, cryogenically cooled, Yb,Na:CaF_2 amplifier”, Opt. Lett. 34, 2075-2077 (2009).

[Raizer] Y.P. Raizer “Gas discharge physics”, Springer (1991).

[Ripoche97] J.-F. Ripoche, G. Grillon, B. Prade, M. Franco, E. Nibbering, R. Lange, A. Mysyrowicz, “Determination of the time dependence of n_2 in air”, Opt. Comun. 135, 310-314 (1997).

[Rockwood73] S. Rockwood, “Elastic and Inelastic Cross Sections for Electron-Hg Scattering Rom Hg Transport Data”, Phys. Rev. A 8, 2348 (1973).

[Talebpour99] A. Talebpour, J. Yang, S.L. Chin, ” Semi-empirical model for the rate of tunnel ionization of N_2 and O_2 molecule in an intense Ti:sapphire laser pulse”, Opt. Commun. 163, 29 (1999).

[Varma08] S. Varma, Y.-H. Chen, H. M. Milchberg, “Trapping and Destruction of Long-Range High-Intensity Optical Filaments by Molecular Quantum Wakes in Air”, Phys. Rev. Let. 101, 205001 (2008).

[Varma12] S. Varma, Y.-H. Chen, J. P. Palastro, A. B. Fallahkair, E. W. Rosenthal, T. Antonsen, H. M. Milchberg, “Molecular quantum wake-induced pulse shaping and extension of femtosecond air filaments”, Phys. Rev. A 86, 023850 (2012).

[Yao11] J. Yao, B. Zeng, H. Xu, G. Li, W. Chu, J. Ni, H. Zhang, S. L. Chin, Y. Cheng, Z. Xu, “High-brightness switchable multiwavelength remote laser in air”, Phys. Rev. A **84**, 051802(R) (2011).

[Yao13] J. Yao, G. Li1, C. Jing, B. Zeng, W. Chu, J. Ni, H. Zhang, H. Xie, C. Zhang, H. Li, H. Xu, S. L. Chin, Y. Cheng, Z. Xu, “Remote creation of coherent emissions in air with two-color ultrafast laser pulses”, New Journ. of Phys. 15**,** 023046 (2013).

[Zeidler01] D. Zeidler, S. Frey, K. L. Kompa, and M. Motzkus, “Evolutionary algorithms and their application to optimal control studies” Phys. Rev. A 64, 023420 (2001).